Northumbria Research Link

Northumbria University
NEWCASTLE

UniversityLibrary

RESEARCH ARTICLE

ESPL **WILEY**

Modelling post-earthquake cascading hazards: Changing patterns of landslide runout following the 2015 Gorkha earthquake, Nepal

Mark E. Kincey[1,2] | Nick J. Rosser[1] | Alexander L. Densmore[1] |
Tom R. Robinson[3] | Ram Shrestha[4] | Dammar Singh Pujara[4] | Pascal Horton[5,6] |
Zuzanna M. Swirad[1,7] | Katie J. Oven[8] | Katherine Arrell[1]

[1]Institute of Hazard, Risk, and Resilience and Department of Geography, Durham University, Durham, UK

[2]School of Geography, Politics and Sociology, Newcastle University, Newcastle upon Tyne, UK

[3]School of Earth and Environment, University of Canterbury, Christchurch, New Zealand

[4]National Society for Earthquake Technology-Nepal, Kathmandu, Nepal

[5]Terranum Sàrl, Bussigny, Switzerland

[6]Institute of Geography & Oeschger Centre for Climate Change Research, University of Bern, Bern, Switzerland

[7]Institute of Geophysics, Polish Academy of Sciences, Warsaw, Poland

[8]Department of Geography and Environmental Sciences, Northumbria University, Newcastle-Upon-Tyne, UK

Correspondence
Mark Kincey, School of Geography, Politics and Sociology, Newcastle University, Newcastle upon Tyne, NE1 7RU, UK.
Email: mark.kincey@newcastle.ac.uk

Abstract

Coseismic landslides represent the first stage of a broader cascading sequence of geohazards associated with high-magnitude continental earthquakes, with the subsequent remobilization of coseismic landslide debris posing a long-term post-seismic legacy in mountain regions. Here, we quantify the controls on the hazard posed by landslide remobilization and debris runout, and compare the overlap between areas at risk of runout and the pattern of post-seismic landslides and debris flows that actually occurred. Focusing on the 2015 M_w 7.8 Gorkha earthquake in Nepal, we show that the extent of the area that could be affected by debris runout remained elevated above coseismic levels 4.5 years after the event. While 150 km^2 (0.6% of the study area) was directly impacted by landslides in the earthquake, an additional 614 km^2 (2.5%) was left at risk from debris runout, increasing to 777 km^2 (3.2%) after the 2019 monsoon. We evaluate how this area evolved by comparing modelled predictions of runout from coseismic landslides to multi-temporal post-seismic landslide inventories, and find that 14% (85 km^2) of the total modelled potential runout area experienced landslide activity within 4.5 years after the earthquake. This value increases to 32% when modelled runout probability is thresholded, equivalent to 10 km^2 of realized runout from a remaining modelled area of 32 km^2. Although the proportion of the modelled runout area from coseismic landslides that remains a hazard has decreased through time, the overall runout susceptibility for the study area remains high. This indicates that runout potential is changing both spatially and temporally as a result of changes to the landslide distribution after the earthquake. These findings are particularly important for understanding evolving patterns of cascading hazards following large earthquakes, which is crucial for guiding decision-making associated with post-seismic recovery and reconstruction.

KEYWORDS
cascading hazards, coseismic landslides, post-seismic runout, remobilization, susceptibility

1 | INTRODUCTION

Earthquakes in mountainous regions can generate significant numbers of coseismic and post-seismic landslides, releasing large volumes of loose sediment and triggering a complex chain of cascading hazards that include debris flows, sediment aggradation, and flooding (e.g., Dahlquist & West, 2019; Fan et al., 2019; Pearce & Watson, 1986; Robinson & Davies, 2013). These landslides can

remain active for several years as debris is remobilized by subsequent rainfall, resulting in the expansion and extension of the original landslide extent (Fan, Domènech, et al., 2018; Kincey et al., 2021). The hazards posed by this remobilization process represent a significant, but generally unquantified, proportion of total landslide hazard experienced in post-earthquake landscapes.

Because the spatial distribution, extent, and stability of individual active landslides change significantly through time, through both the remobilization of existing landslides and the formation of new post-seismic landslides (Fan, Domènech, et al., 2018; Kincey et al., 2021; Marc et al., 2019), the future hazard posed by the runout of debris must also change accordingly. Critically, thresholds for landslide triggering may also reduce, rendering previously safe areas hazardous (e.g., Dadson et al., 2004), and the most prevalent mass wasting mechanisms may shift to become more dominated by debris flows (Zhang & Zhang, 2017). Importantly, much of the coseismic landslide debris may also lie upstream of the channel network (Li et al., 2016) and so can run out over areas that have not previously experienced landslides or debris flows. Thus, the evolving landslide hazard after a large earthquake consists of at least four distinct components: (1) remobilization of coseismic debris, (2) continued failure of coseismic landslides, (3) new post-seismic landslides on previously-unfailed hillslopes, and (4) remobilization of post-seismic debris. Understanding the changing significance of each of these different components of the hazard chain should therefore be a fundamental aspect of any comprehensive assessment of post-seismic risk.

Previous studies assessing the post-seismic evolution of landslide hazard have focused on the analysis of multi-temporal landslide inventories to assess changes to existing failure extents, the occurrence of new post-seismic landslides, or both (e.g., Fan et al., 2019; Fan, Domènech, et al., 2018; Fan, Zhang, et al., 2018). For example, after the 2015 M_w 7.8 Gorkha earthquake in Nepal, such an analysis has demonstrated that 3.5 years after the earthquake, landslides remained more numerous and covered a larger total area than they did on the day of the earthquake (Kincey et al., 2021). Importantly, the changing post-seismic landslide distribution comprised both persistently-active coseismic landslides but also new post-seismic landslides that had developed since the earthquake; thus, the sources of landslide debris with the potential to runout must change over time. Similarly, in the years following the 2008 M_w 7.9 Wenchuan earthquake in China, the primary hillslope failure mechanism shifted from landslides to debris flows, with Huang and Li (2014) documenting a landslide/debris flow ratio of 5:1 for the pre-seismic period and 1:1 for the initial 5-year post-seismic period. This increase in debris flow prevalence reflected the abundance of loose coseismic debris and the associated reduction in the hydrological triggering threshold required for mobilization (Fan, Zhang, et al., 2018; Ma et al., 2017). The post-seismic increase in debris flow occurrence reduced through time, potentially as a result of progressive exhaustion of supply (Qu, 2019; Yunus et al., 2020), grain coarsening due to the loss of fine sediment (Domènech et al., 2019), or revegetation of failure scars (Shen et al., 2020; Yang et al., 2018). Debris-flow runout distances have also generally decreased through time, perhaps due to a reduction in sediment mobility and downslope progression of debris flow initiation positions (Fan, Zhang, et al., 2018; Zhang & Zhang, 2017).

However, the time period over which increased debris mobilization persists after an earthquake appears to vary considerably between both settings and studies. In their study of post-seismic debris flows in the 2 years following the Gorkha earthquake, Dahlquist and West (2019) suggested that there was only a short-lived transient increase in debris flow rates, with the available coseismic sediment supply being largely exhausted during the first monsoon and a reduction in the number of new debris flows back to pre-seismic levels within a year. This rapid return to pre-seismic conditions was argued in part to be due to the low proportion (∼2%) of coseismic landslides that actually transitioned into post-seismic debris flows (Dahlquist & West, 2019; Roback et al., 2018). In contrast, more recent and longer-term studies of post-seismic hillslope evolution following the Gorkha earthquake have indicated that landslide and debris flow hazards are still high relative to pre-seismic conditions. For example, in their field-based study of landslide development during the period 2015–2018, Tian et al. (2020) documented repeated activity and continued hazard across the majority of the investigated sites, with a notable shift in the dominant failure mechanism towards debris flows. Similarly, the 2020 monsoon is known to have triggered extensive debris flows across large areas of central Nepal that were badly affected by the Gorkha earthquake (Rosser et al., 2021), suggesting a persistent runout hazard legacy associated with the earthquake. This persistence has been noted after the Wenchuan earthquake as well, and has been ascribed to an abundance of coseismic sediment even years after the earthquake (Huang & Li, 2014; Zhang & Zhang, 2017), changing source area form and location (Li et al., 2018; Zhang et al., 2016) and spatio-temporal variability in triggering factors such as high rainfall events (Ma et al., 2017; Yunus et al., 2020).

A limitation of most current approaches to assessing changing landslide and debris-flow hazard after a large earthquake is that they have focused on mapping where landslides have already occurred, resulting in limited capacity to predict how the hazard will evolve. An alternative approach is to forecast the potential evolution of the hazard footprint using a runout model, and then to compare modelled outputs with multi-temporal inventories to assess and refine the runout model based on where the modelled hazard has been 'realized'. Because we cannot reliably identify which landslides are likely to be remobilized at the full event scale, a precautionary approach is to assume that further runout of any landslide source remains possible. Typical approaches are to model potential runout pathways based on manually-mapped landslides as potential source areas (Aaron et al., 2019), or to use a predicted source area distribution based on predefined variables (Kappes et al., 2011; Pastorello et al., 2017) or a threshold-based landslide susceptibility model (Melo & Zêzere, 2017; Paudel et al., 2020). Such assessments usually provide a snapshot of the hazard, and it is hard to test or update the hazard due to a lack of multi-epoch landslide inventories that describe how the landslide footprint evolves. Whilst one-off regional-scale debris flow hazard assessments are commonplace (e.g., Blais-Stevens & Behnia, 2016), the degree to which runout occurs during the initial mass movement versus during reactivation remains poorly understood, and so is difficult to account for in hazard assessments.

To address these issues, we use multi-epoch landslide inventories from the 2015 Gorkha earthquake (Kincey et al., 2021) to assess the changing extent of potential runout from coseismic and post-seismic landslides in the 4.5 years following the earthquake. We use Flow-R, a spatially distributed empirical model for regional-scale estimation of

debris runout (Horton et al., 2013), to model the spatial footprint of potential runout across the area that was most affected by the earthquake, using mapped landslides as source areas. We repeat this simulation based upon 13 separate epochs of landslide mapping at approximately 6-month intervals (2014–2019) and compare modelled runout to subsequent mapped landslides. This approach allows us to explore how changes in the spatial distribution and character of landslides influence the evolution of post-earthquake landslide runout and the degree to which landslides achieve or 'realize' the modelled runout, and to identify the controls on that realization of runout potential. We use this information to derive a synoptic overview of the evolution of post-earthquake landslide runout and to describe the regional-scale characteristics of landslide runout pathways, which together provide inputs into a more holistic understanding of the long-term hazard chain associated with earthquake-triggered landslides.

2 | METHODS

2.1 | Landslide inventory mapping

Landslides were manually mapped from medium-resolution satellite imagery (Landsat 8, with a spatial resolution of 30 m pan-sharpened to 15 m for 2014–2015; Sentinel-2, with a spatial resolution of 10 m for 2016–2019) across a 24,402 km^2 area of central Nepal that was most severely impacted by the 2015 Gorkha earthquake (Figure 1a). A total of 13 individual landslide epochs covered the period from 2014 to 2019, including pre- and post-monsoon inventories for each year and an additional coseismic inventory for 2015. Landslide footprints incorporated both source areas and deposits due to the resolution of the satellite imagery. Assigning levels of post-failure reactivation and remobilization using remotely-sensed imagery is not straightforward (e.g., Fan, Domènech, et al., 2018) and so we mapped all landslides visible in each epoch independently, irrespective of whether they were

already present within a preceding inventory. This approach is necessary since mapping only new or substantially-altered landslides in each epoch would have removed persistent landslides which could potentially act as source zones for later runout from the analyses. Our approach therefore makes the assumption that bare, unvegetated ground equates to the presence of exposed rock or sediment that could be mobilized in a future event, which is justified based on field observations (Tian et al., 2020) and a precautionary approach to modelling cascading hazards across such a large spatial area (Kincey et al., 2021). A detailed description of our mapping approach and its implications for time series analysis of modelled runout is provided in Supporting Information Methods S1, while full details of the multi-temporal landslide inventory construction and analysis are provided by Kincey et al. (2021).

2.2 | Runout modelling

To assess the potential runout from existing landslides, we used the flow path assessment of gravitational hazards at a regional scale (Flow-R) model version 2.0 (Horton et al., 2013). Flow-R is a spatially distributed empirical model designed to model runout paths across large spatial extents with minimum input data requirements. Runout paths from defined source areas – here manually mapped landslides – are propagated on the basis of a spreading algorithm that controls the route and extent of the flow, and friction laws that determine the runout distance. The flow volume and mass are not directly considered, as these cannot be accurately quantified across large regions. Instead, the model is well-suited to regional susceptibility assessments where the full range of possible runout pathways from a large set of distributed sources must be considered. Flow-R has been utilized in a range of different applications, including debris flow hazard assessments in Switzerland (Horton et al., 2008), France (Kappes et al., 2012), Italy (Blahut et al., 2010) and Norway (Fischer et al., 2012), as well as
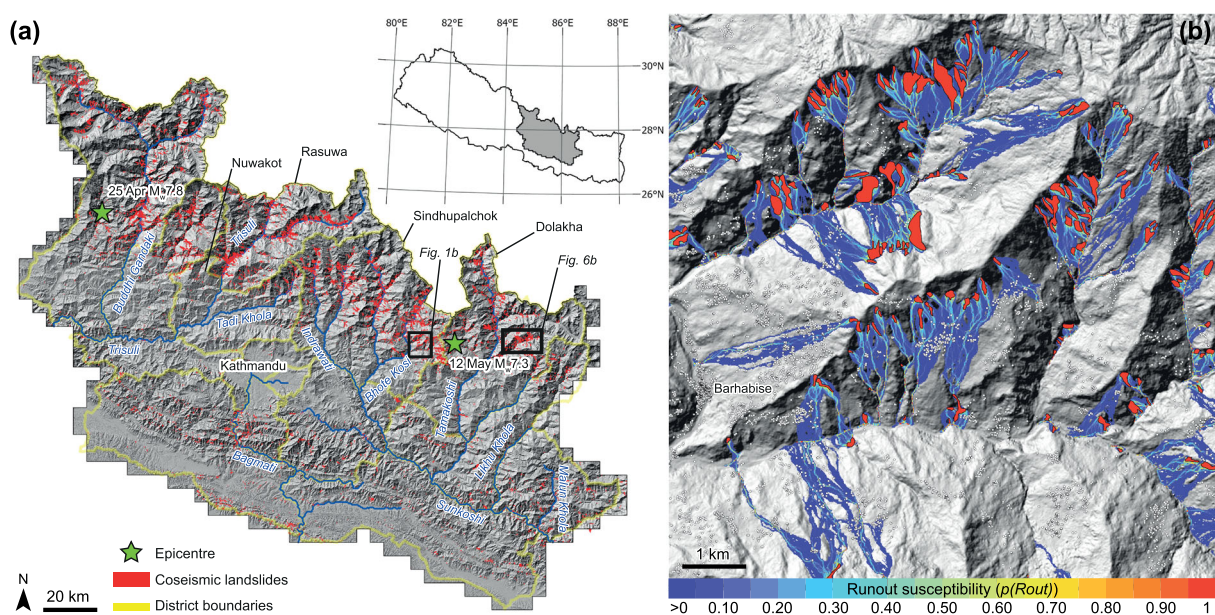
FIGURE 1 (a) Location of study area showing the coseismic landslide distribution (Epoch 4) in red. (b) Extract from the runout model (*Rout_Mod*) results showing maximum runout susceptibility (*p(Rout)*) from coseismic sources (*Ls_Map*; shown in red) (AW3D 5 m DEM ©JAXA, RESTEC and NTTDATA). [Color figure can be viewed at wileyonlinelibrary.com]

modelling other gravitational hazards such as rockfall (Losasso et al., 2016; Michoud et al., 2012), snow avalanches (Horton et al., 2009; Jaboyedoff et al., 2012) and rock avalanches (Oppikofer et al., 2016).

Runout modelling used the 13 manually-mapped landslide inventories to sequentially define the potential source areas (Section 2.1) and a 10 m digital elevation model (DEM), resampled from a 5 m resolution Advanced Land Observing Satellite World 3D (AW3D) dataset, as the most appropriate compromise between accuracy of modelled flow paths, reduction of topographic noise, and processing time (Claessens et al., 2005; Fischer et al., 2012; Horton et al., 2013) (see Methods S2 for full details of the Flow-R model inputs and parameters). In this configuration, the model is testing the potential for runout from the full landslide footprint, including continued runout from the landslide source and the potential for remobilization of the deposit.

For our analyses, spreading of the runout path was based on a modified version of Holmgren's multiple flow direction algorithm (Holmgren, 1994) that includes an additional height factor ($dh = 1$ m) designed to increase the elevation of the central processing cell and so account for any height errors in the DEM (see Horton et al., 2013). Flow inertia was simulated by weighting the flow direction based on the change in direction with respect to the previous cell using the Gamma implementation of Horton et al. (2013). Runout distances were quantified using a simplified friction-limited model based on the maximum possible runout distance, controlled by a user-defined minimum travel angle, also termed the angle of reach or fahrböschung angle. Based on published field observations of debris flows, we selected a minimum travel angle of $11°$ and a maximum flow velocity of 15 m s^{-1}, which is required in order to restrict the flow energy to realistic limits and therefore avoid improbable runout distances (see full discussion in Horton et al., 2013).

Tuning of model input parameters to fit individual landslides was not appropriate given the regional scale of the study area (> 24,000 km^2) and the number and variability of source areas used in the modelling (> 195,000 landslides). Our parameterization of the model was therefore based on input values that have been developed for modelling runout in similar mountainous terrain by previous studies, and through initial testing of the model to generate plausible runout pathways (see Methods S4). Sensitivity analysis of the different parameters for a subset area located in Sindhupalchok district, central Nepal (Supporting Information Figure S3), showed that the Holmgren exponent value (x) is the most sensitive parameter in terms of influencing the overall modelled runout extent and susceptibility distributions. The travel angle and velocity threshold values determine the degree to which flow is permitted to continue downslope, but the results were relatively insensitive to the choice of the height factor (dh). The sensitivity analysis shows that our parameter choices represent a plausible but precautionary approach to the modelling of runout, which is appropriate given the potential implications of the work in terms of risk to life and livelihood (Methods S4). Sensitivity testing showed that variations in modelled runout extent vary by at most 43% depending on specific parameter choices, but most parameter sets (70%) are within 10% of the runout area modelled by this study (Supporting Information Table S3).

For every 10 m × 10 m cell, the model assigned a susceptibility value $p(Rout)$ with a value from 0 (no chance of being within a runout path) to →1 (very likely to be within a runout path). Landslide areas had a value of 1. The model accounted for cells located within multiple modelled runout pathways, from which a set of summary statistics were generated, including: maximum runout susceptibility from all upslope sources combined (Figure 1b); the sum of all runout susceptibilities, which assesses total runout susceptibility irrespective of source; and runout count, which accumulates the number of distinct sources that could impact a cell irrespective of susceptibility. We refer to the locus of cells where $p(Rout) > 0$ as Rout_Mod. The sequential model runs based on the 13 multi-temporal landslide inventories allowed an assessment of how Rout_Mod changed over the 4.5 years since the 2015 earthquake.

2.3 | Time series analysis

Quantitative assessment of model performance using standard error statistics is somewhat complicated because Flow-R is a forward model, and runout from existing landslide source locations is time- and trigger-dependent. Thus, the occurrence or non-occurrence of actual runout for any given cell at a single point in time does not simply indicate model success or failure. In other words, the lack of realized runout does not show that the model failed in its prediction, because the actual occurrence of runout may still happen in the future if there is a sufficient trigger event. This study is therefore focused on an assessment of how the runout distribution and realization change through time after an earthquake, using a precautionary but plausible modelling approach.

We first assessed the net change in Rout_Mod across the study area using aggregate statistics, per-cell values, and frequency distributions of $p(Rout)$ for each epoch in turn. All cells mapped as landslides are referred to as Ls_Map, with any cell classified as Ls_Map relating to a model source location for that epoch and so excluded from the associated list of Rout_Mod runout cells. We refer to cells in Rout_Mod that experienced landsliding in later epochs, which we term 'realization' of the modelled runout, as Rout_Real. For each epoch, each 10 m × 10 m cell in Rout_Mod was categorized based on whether it became part of a landslide during that epoch (i.e., the cell was contained within Ls_Map and so it became part of Rout_Real), remained within the modelled runout extent (the cell remained in Rout_Mod but outside of Ls_Map), or no longer fell within the modelled runout extent (i.e., $p(Rout) = 0$), which typically occurred when the associated upslope landslide became revegetated and was no longer visible as bare ground. This process was repeated for each epoch, allowing the stepwise evolution of Rout_Mod and the match between this and Ls_Map to be assessed (see Methods S3 for additional description of the runout variables described above).

Since our analysis considered realized runout to include any cells within a modelled runout area that experienced landsliding in later epochs, this realization could plausibly occur as a result of both changes to pre-existing landslides and the occurrence of entirely new landslides. This approach is justified from the perspective of informing a comprehensive post-seismic hazard analysis, but it is still important to also consider what proportion of realization comes from existing landslides versus entirely new landslides. To calculate this, we used a series of spatial selection queries to identify which landslides had a direct physical intersection with earlier landslides and considered

these to be pre-existing landslides. Any landslides that had no intersection with landslides from earlier epochs were classified as entirely new landslides (see Methods S10 for full methodological details).

Note that the percentage of *Rout_Mod* that is realized by the end of each epoch – that is, the ratio of *Rout_Real* to *Rout_Mod* – is equivalent to the model precision. We would expect this quantity to change over time, as runout proceeds and as areas within *Rout_Mod* that are downslope of existing landslides become inundated with debris. Similarly, we would expect the model recall – the ratio of *Rout_Real* to the sum of *Rout_Real* and any new landslides that occur outside of the modelled runout area – to also change over time, as new landslides occur outside of *Rout_Mod*. We thus assessed model performance using sequential precision-recall curves, which are preferable to other performance measures when *Rout_Mod* is a small fraction of the overall area (e.g., Saito & Rehmsmeier, 2015). We used Flow-R to calculate *Rout_Mod* using the coseismic landslide footprints (Epoch 4) as the runout source areas, and evaluated model precision and recall up to that point in time after each subsequent epoch. For this portion of the analysis, we treated realization as a cumulative process; that is, we considered that a cell in *Rout_Mod* was realized if it appeared as a landslide in a subsequent epoch, even if the cell was not mapped as a landslide in later epochs. This avoids complications caused by vegetation growth or obstruction of the ground surface in some but not all epochs (see Kincey et al., 2021).

To assess broader spatial variability in *Rout_Mod, Ls_Map, and Rout_Real*, we generated a set of geomorphological slope units across the study area, based on the methodology developed by Alvioli et al. (2016). This approach uses a DEM to partition a landscape into individual terrain units that are defined by hydrological and geomorphological boundaries (Alvioli et al., 2020), and has been shown to be appropriate for susceptibility assessments across large spatial areas (Domènech et al., 2020; Jacobs et al., 2020; Tanyas et al., 2019). The size distribution of output slope units is primarily determined by parameters controlling the flow accumulation thresholds and the circular variance in terrain aspect that is permitted within a single slope unit, which together define the acceptable degree of aspect homogeneity between adjacent units. Slope units were generated within Grass GIS version 7.8.4 using the minimum parameter settings from the range of values recommended by Alvioli et al. (2016) which delimit slope units to a scale that matches observed approximate hillslope length scales across the study area (see Methods S5 for full details of slope unit parameters). Each resulting slope unit ($n = 13,456$) was attributed with a range of landslide and runout statistics for each mapping epoch, including: the number of landslides, the total area of landsliding, the total modelled runout area, and statistics summarizing the maximum and summed runout susceptibilities (minimum, maximum, range, mean, sum, standard deviation). All of the topographic and environmental variables were also aggregated to each slope unit as tabular attributes using the same set of summary statistics as were used for the runout susceptibility values.

2.4 | Identifying locations favourable for landslide runout

Analysis of potential controls on runout evolution and hazard realization focused on eight topographic variables that have previously been

shown to influence the occurrence of coseismic and post-seismic hillslope landslides: elevation, slope, aspect, normalized distance to stream channel, profile and plan curvature, upslope contributing area, and Melton ratio (defined here as per-slope unit relief divided by the square root of slope unit area) (e.g., Kincey et al., 2021; Parker et al., 2015; Robinson et al., 2017). Three event-specific variables from the Gorkha earthquake were also included: slope aspect relative to the epicentre, the Euclidean distance to the epicentral location, and the distance to the nearest mapped coseismic landslide. All control variables were analysed at 10 m resolution using the same AW3D DEM (see Methods S6 for full details of the potential control variables).

The significance of each variable was assessed in two ways: by (1) comparing per-slope unit aggregated summary statistics of each variable (see Section 2.3) to corresponding modelled runout areas and realization percentages, and (2) cell-by-cell differencing of kernel density estimations for all control variables at 10 m resolution. Since the Melton ratio was calculated for each slope unit, analysis of this metric was conducted at this scale only. For the cell-based analysis, separate kernel density estimates were generated for modelled coseismic runout cells that became landslides in any subsequent epoch (i.e., *Rout_Real*), and for cells which did not (i.e., cells which remained in *Rout_Mod* or later became $p(Rout) = 0$), and these were then differenced from kernel density estimates based on all cells within the modelled coseismic runout extent (*Rout_Mod*). Negative density difference values indicate that the sub-population at that value of the control variable occurs less frequently than would be expected from the overall modelled runout extent, and positive values meaning the sub-population at that value occurs more frequently. A full description of the kernel density differencing methodology is provided in Kincey et al. (2021).

3 | RESULTS

3.1 | Characteristics of post-earthquake runout evolution

Evolution of landslide area (*Ls_Map*) in the pre-seismic, coseismic, and post-seismic phases was described by Kincey et al. (2021), so we provide only a brief summary here. The total landslide area for the three pre-earthquake epochs was consistently low, ranging between 60 and 64 km^2, equivalent to 0.2–0.3% of the overall study area (Figure 2; Methods S7). This increased substantially after the 2015 Gorkha earthquake, reaching 150 km^2 (0.6% of the study area) for the coseismic inventory and 174 km^2 (0.7%) for the post-monsoon 2015 inventory. Landslide area generally decreased through post-monsoon 2017 (Epoch 9), when it reached a minimum value of 131 km^2 (0.5%). In contrast, the period from pre-monsoon 2018 to post-monsoon 2019 showed an increasing trend, with landslide areas totalling 155 km^2 (0.6%) in the final inventory of the time series (Epoch 13). This represents the highest total since early 2016 and was 5 km^2 (~3%) greater than the equivalent coseismic landslide area.

Overall modelled runout extents (*Rout_Mod*) broadly follow the same pattern as the mapped landslide areas (Figure 2). Pre-seismic *Rout_Mod* extents ranged between 245 and 258 km^2 (1.0–1.1% of the study area), increasing to 614 km^2 (2.5%) with the 2015 earthquake
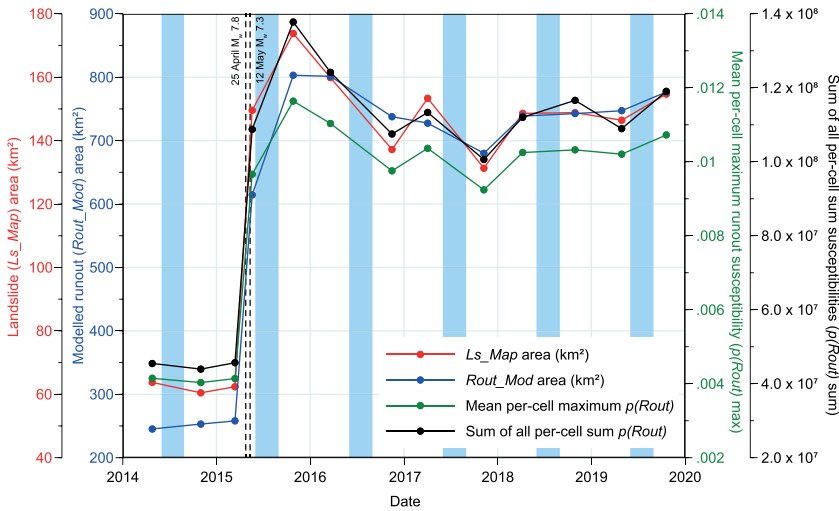
FIGURE 2 Time series of total landslide area (Ls_Map), runout area (Rout_Mod), and runout susceptibilities (p(Rout)) for the overall study area. Vertical blue bars show the timing of the monsoon; dashed vertical black lines indicate the dates of the 25 April M_w 7.8 Gorkha earthquake and the 12 May M_w 7.3 aftershock. Modified from Kincey et al. (2021) and Rosser et al. (2021). [Color figure can be viewed at wileyonlinelibrary.com]
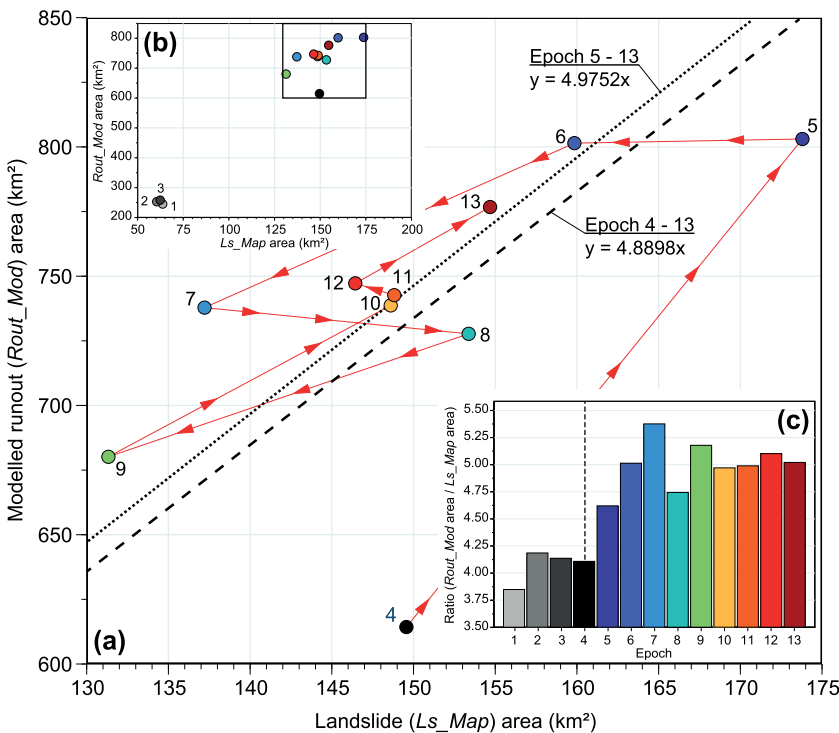

FIGURE 3 (a) Correlation between per-epoch landslide (Ls_Map) area and modelled runout (Rout_Mod) area. Separate trend lines fitted for (1) Epochs 4–13, dashed, and (2) Epochs 5–13, dotted, with regression lines both forced through the origin. The red line connects the epochs sequentially by date to indicate changes through time. Panel (b) shows the same data but including the three pre-earthquake Epochs 1–3. (c) Ratio of modelled runout (Rout_Mod) area to landslide (Ls_Map) area through time. Higher values indicate greater runout extent relative to the landslide sources. Vertical black dashed line indicates the time of the earthquake (Epoch 4). [Color figure can be viewed at wileyonlinelibrary.com]

and reaching a maximum of 803 km^2 (3.3%) for the post-monsoon 2015 inventory. Rout_Mod extents then decreased to post-monsoon 2017, when a minimum runout area of 680 km^2 (2.8%) was recorded. The area of Rout_Mod then increased to 777 km^2 (3.2%) in post-monsoon 2019, ~26% greater than the total modelled coseismic runout extent.

Per-epoch Rout_Mod extents show a clear correlation with the equivalent per-epoch landslide areas (Figure 3), indicating that the size of the potential runout area can be broadly anticipated based on the area of visible landsliding. The relationship between runout area and landslide area differs, however, depending on whether the coseismic data are included (Figure 3a,b). This difference is also apparent when the ratio of Rout_Mod area to Ls_Map area is considered (Figure 3c). The total Rout_Mod area for the coseismic inventory is approximately four times larger than the coseismic Ls_Map area, which is broadly consistent with the average ratio for the three pre-seismic epochs. In contrast, for post-seismic epochs this ratio increases, with Rout_Mod

areas being on average five times larger than their equivalent Ls_Map areas. The magnitude of differences between per-epoch Rout_Mod area and Ls_Map area converge through time to a near-constant ratio when considered sequentially (red line on Figure 3a).

Modelled p(Rout) values – that is, the likelihood that a cell sits within a modelled runout path – show the same trend as the landslide and runout areas when analysed as both mean per-cell maxima and the total sum of all runout susceptibilities (Figure 2). Both p(Rout) metrics increased substantially with the earthquake and peaked in post-monsoon 2015 (Epoch 5), before decreasing through post-monsoon 2017 (Epoch 9) and then increasing again to the end of the study period. The distribution of p(Rout) also shifted from pre- to post-earthquake epochs (Figure 4). Pre-earthquake values of p(Rout) were generally higher than coseismic values, reflecting the small number of pre-earthquake landslides which tended to occur in areas close to the channel network and thus prone to remobilization and runout (Kincey et al., 2021). After the earthquake and subsequent monsoon, there
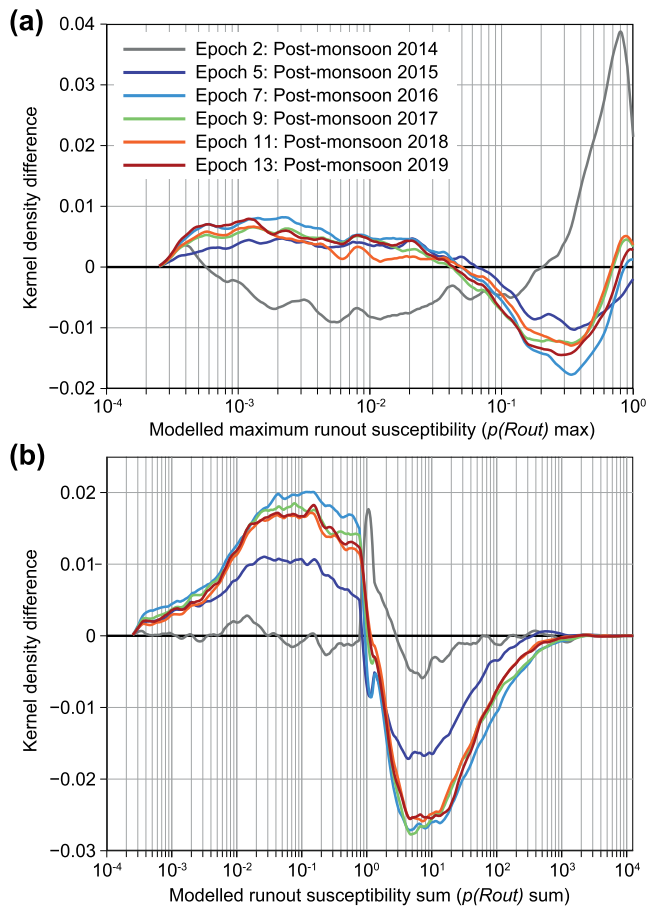
FIGURE 4 Kernel density estimates of the distributions of (a) maximum per-cell runout susceptibility ($p(Rout)$ max) and (b) the per-cell sum of all runout susceptibilities ($p(Rout)$ sum), expressed as the difference between each distribution and the coseismic distribution in Epoch 4 (black line). Positive values represent a greater number of cells with corresponding value of $p(Rout)$, negative value represent a smaller number of cells relative to Epoch 4. [Color figure can be viewed at wileyonlinelibrary.com]

was a notable increase in low to intermediate values of $p(Rout)$ (Figure 4), which when combined with the larger extent of $Rout\_Mod$ indicates that a broader range of locations in the landscape became susceptible to runout.

3.2 | Post-seismic changes in modelled coseismic runout realization

Although runout susceptibility evolved as a result of changes to the number, distribution, and form of landslides in subsequent post-seismic epochs, it is still valuable to assess the degree to which the potential runout area modelled from just a coseismic landslide inventory was fulfilled in the years following the earthquake. This provides insights into timescales over which a runout assessment carried out in the immediate aftermath of an earthquake might remain relevant, as well as the degree to which the realization of the modelled runout area varies under different model susceptibility thresholds.

We focus initially on the modelled runout area $Rout\_Mod$ from the coseismic landslides (Epoch 4). When all modelled runout susceptibility values are included, 14% (85 km²) of $Rout\_Mod$ cells from coseismic landslides became $Rout\_Real$ at some point in the 4.5 years
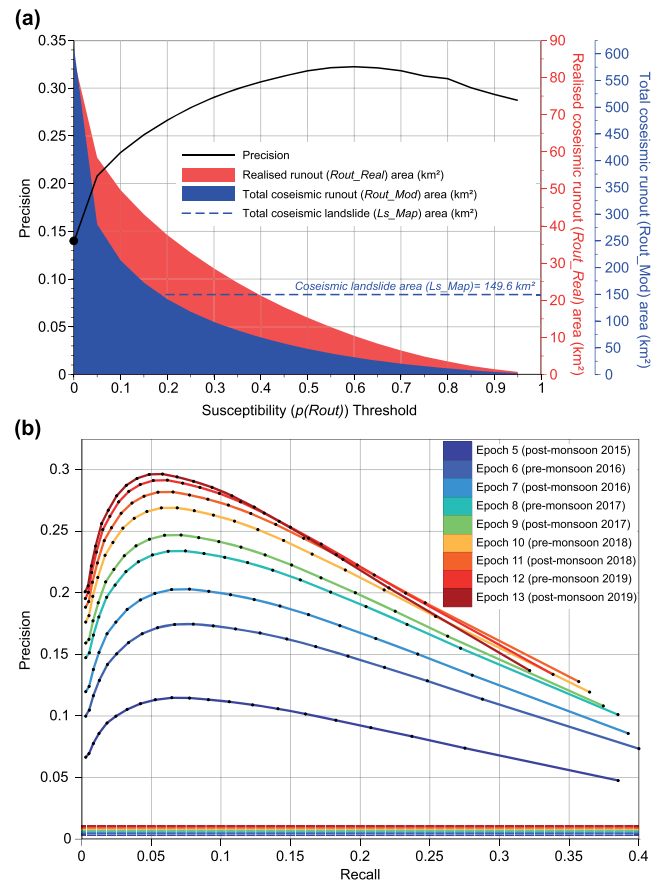
FIGURE 5 (a) Area of modelled coseismic runout ($Rout\_Mod$; blue) and area of modelled coseismic runout that was realized by landslide occurrence within any post-EQ epoch ($Rout\_Real$; red), as a function of modelled susceptibility $p(Rout)$ threshold. The black line shows the model precision, defined as the realized runout area ($Rout\_Real$) as a fraction of the total coseismic runout area ($Rout\_Mod$), again as a function of susceptibility ($p(Rout)$ threshold. The maximum model precision occurs at a $p(Rout)$ threshold of 0.6. Black dot on the y-axis indicates that 14% of all coseismic $Rout\_Mod$ was realized by the end of the study. (b) Precision-recall curves for each of the post-seismic epochs, based on modelling of runout from coseismic (Epoch 4) landslides and comparison with subsequent mapped landslide inventories (Epochs 5–13). Each curve is calculated based on the cumulative extent of post-seismic landsliding that occurred up until that epoch. Black dots along the curve represent the susceptibility thresholds, increasing in 0.05 intervals from zero. Horizontal dashed lines towards the base of the y-axis show the no skill values for a random classifier from each epoch; note that the precision depends upon the number of positive values, and so varies between epochs. [Color figure can be viewed at wileyonlinelibrary.com]

after the 2015 earthquake (Figure 5a). In other words, 86% of the modelled hazard remained 'unrealized' by the end of the study. This is a highly conservative test of the runout model, as cells with very low susceptibilities are included. We therefore apply a moving threshold to progressively examine the evolution of cells with higher values of $p(Rout)$. As this threshold increases, whilst the area of $Rout\_Mod$ naturally decreases, $Rout\_Real$ initially increases (black line on Figure 5a), indicating increased model precision. This is greatest for a $p(Rout)$ threshold of ≥ 0.6, at which 32% (10 km²) of all modelled coseismic runout cells (32 km²) became a landslide at some point during our study period. The percentage of $Rout\_Mod$ cells that were realized decreases marginally for higher thresholds, but this also leads to a pronounced decrease in the predicted runout area (Figure 5a); for

example, only 2.5 km^2 of runout is modelled if we assume a threshold of $p(Rout) = 0.95$.

Inspection of precision-recall curves evaluated after each epoch shows that model precision generally increases over time, as expected (Figure 5b), but at a decreasing rate as more of the coseismic *Rout_Mod* was progressively realized. Precision is maximized at $p(Rout)$ values of 0.5–0.6. For all epochs, the model is considerably more skilled than a random classifier (Figure 5b). Note, however, that maximum model recall values decrease somewhat in later epochs, likely due to the occurrence of new landslides that do not fall within the coseismic *Rout_Mod*.

Analysis of the intersections between landslides from different epochs shows that 90% of the total post-seismic realization of the coseismic runout area came from landslides that were physically connected to the original coseismic landslide footprints, with only 10% originating from entirely new landslides (Methods S10). When evolving downslope connections between landslides are considered, this value increases to 92% of the realized area being related to pre-existing landslides and only 8% coming from entirely new landslides. In both cases, the proportion of realized runout that is attributable to pre-existing coseismic landslides decreases through time. For direct intersections with coseismic landslides, the values decrease from 91% in post-monsoon 2015 (Epoch 5) to 85% in post-monsoon 2019 (Epoch 13), with the equivalent figures for the evolving downslope connections being 94% and 89% (Figure S14). For all post-seismic epochs combined, we find that 62% of the area impacted by new post-seismic landslides that are directly connected to coseismic landslide polygons is within the modelled runout extent, compared with 38% that is outside of the modelled extent Methods S10. When

analysed through time, we find that the proportion of newly impacted ground that is within the modelled runout extent increases from 61% in post-monsoon 2015 (Epoch 5) to 65% in 2016 (Epochs 6 and 7), before decreasing to 60% by post-monsoon 2019 (Epoch 13) (Figure S15).

3.3 | Runout hazard realization in a changing post-seismic landscape

We next examine the realization of *Rout_Mod* from all coseismic and post-seismic epochs. Disaggregating the realized hazard data by epoch allows us to establish the time between when a cell is first predicted as being within a runout area (*Rout_Mod*) and when it is first intersected by a mapped landslide (*Rout_Real*), here termed the 'realization wait time' (Figure 6; Methods S8 and S9). For the runout area *Rout_Mod* modelled from the coseismic landslide population (Epoch 4), 4.8% of *Rout_Mod* cells are realized after just one epoch (post-monsoon 2015, *c.* 0.5 year wait time), and a further 2.6% after two epochs (pre-monsoon 2016, *c.* 1 year) (Figure 6a; see Figure S12 for an equivalent plot in terms of the area of *Rout_Real* over time). The proportion of *Rout_Mod* cells that become *Rout_Real* in each subsequent epoch then continues to decrease through time, although with notable pre- and post-monsoon fluctuations during 2016 and 2017 in particular. Only 0.3% of the coseismic *Rout_Mod* cells are realized as landslides after nine epochs (~4.5 years). The spatial pattern of realization indicates that hazard realization occurs through various mechanisms, including runout via downslope channelized movement of sediment from a pre-existing landslide, in addition to the occurrence
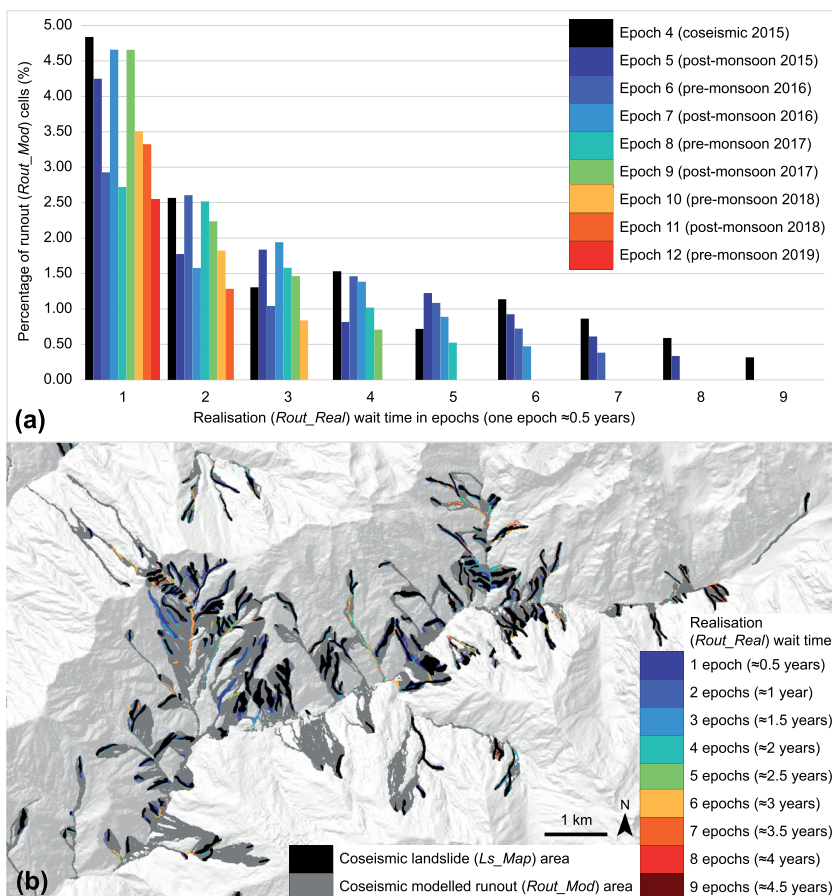
FIGURE 6 (a) Distribution of runout realization wait times for all coseismic and post-seismic epochs. Realization wait times are defined here as the time between when a cell is first included within a modelled runout area for a given epoch (*Rout_Mod*), and when it first intersected a mapped landslide polygon (*Rout_Real*). Note that longer wait times can only be determined for the earlier epochs due to the brevity of our inventory data. (b) Map showing an example of per-cell realization wait times associated with the modelled coseismic runout for an area of Dolakha district. The spatial extent of this map is shown on Figure 1 for reference. [Color figure can be viewed at wileyonlinelibrary.com]

of new landslides within the modelled coseismic runout extent (Figure 6b). Realization of *Rout_Mod* from landslide source areas in subsequent epochs follows a similar trend (Figure 6a).

Although the proportion of the *Rout_Mod* area that remains unrealized decreases through time (Figure 6; Methods S8), total *Rout_Mod* remains high for all post-seismic epochs (Figure 2). This implies that the modelled runout area is shifting spatially, reflecting changes to landslide footprints and the addition of new landslides in later epochs, meaning that the analysis of hazard realization needs to also track changes occurring in individual post-seismic epochs.

FIGURE 7 (a) Extent of modelled runout in each of the mapping epochs that was realized by landslide occurrence within any subsequent epoch (*Rout_Real*), differentiated by susceptibility (*p(Rout)*) threshold. Note: The realization area data on the *y*-axis are stacked. (b) Model precision by epoch, defined as the realized runout area (*Rout_Real*) as a fraction of the total coseismic runout area (*Rout_Mod*), again differentiated by susceptibility (*p(Rout)*) threshold. For all epochs, the model achieves maximum precision at a *p(Rout)* threshold of 0.55–0.65; these points are connected for reference to show their evolution in time for both pre- and post-monsoon inventories. Coloured dots on the *y*-axis indicate the proportion of all *Rout_Mod* that was realized by the end of the study for each mapping epoch. [Color figure can be viewed at wileyonlinelibrary.com]
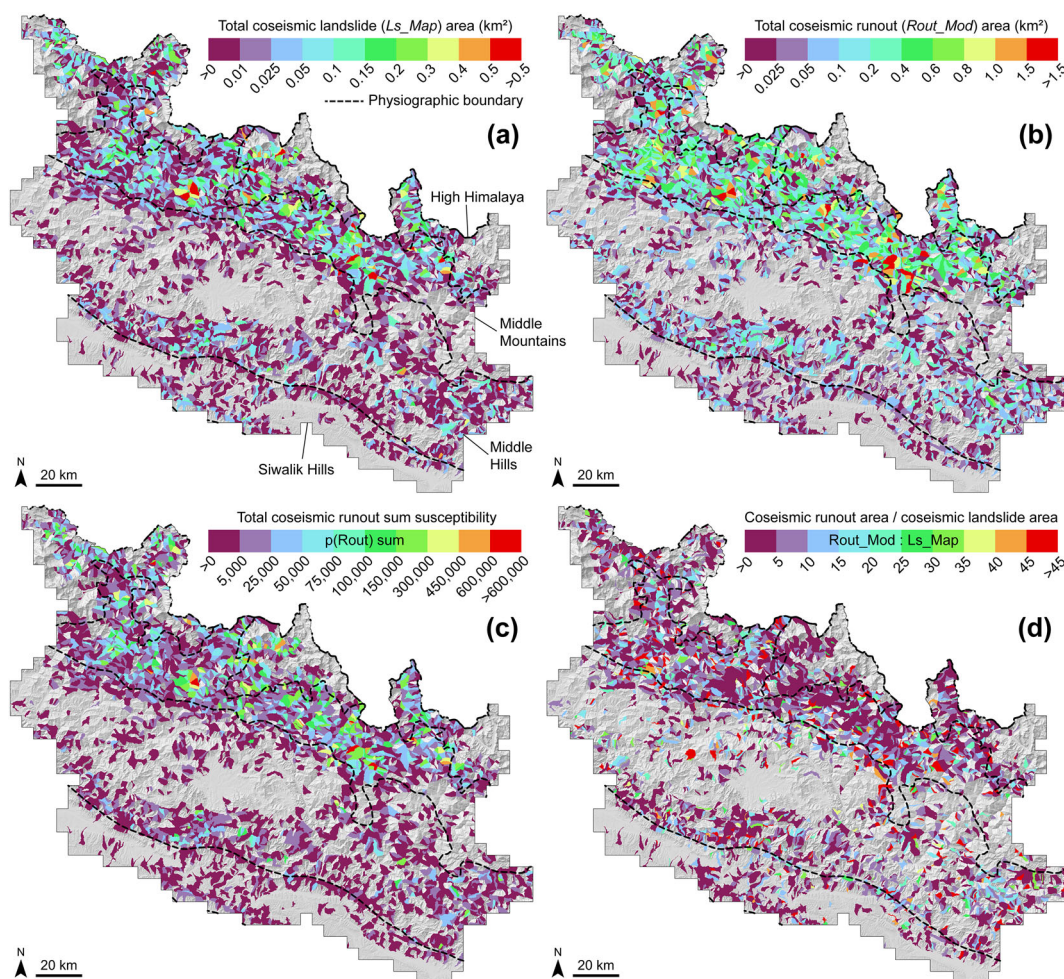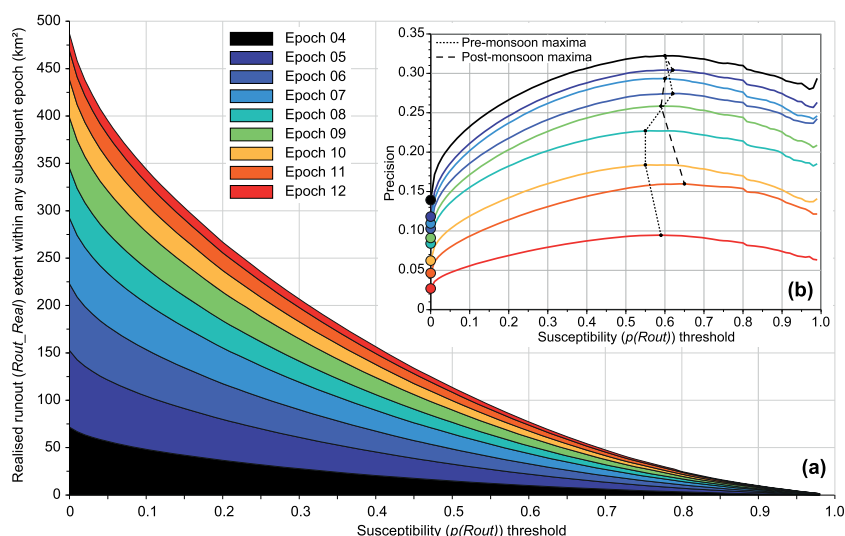
FIGURE 8 Spatial distribution of key runout metrics aggregated by individual slope unit. (a) Total coseismic landslide (*Ls_Map*) area; (b) total modelled coseismic runout (*Rout_Mod*) area; (c) summed susceptibilities (*p(Rout)*) of coseismic runout; (d) ratio of coseismic runout area to landslide area (*Rout_Mod:Ls_Map*). Dashed black lines represent the major physiographic boundaries within the study area. [Color figure can be viewed at wileyonlinelibrary.com]

Not surprisingly, the proportion of the total *Rout_Mod* that eventually becomes *Rout_Real* decreases in successive epochs, from > 10% (∼80 km^2) for post-monsoon 2015 to 3% (∼20 km^2) for pre-monsoon 2019 (Figure 7b). Whilst thresholding *Rout_Mod* at higher *p(Rout)* values yields a smaller runout area in each epoch, the overall pattern of declining realization through time remains (Figure 7a). As with realization of runout from the coseismic landslides (Figure 5), model precision for all epochs is greatest for locations with *p (Rout)* values ≥ 0.6 (Figure 7b). Maximum *Rout_Real* percentages generally decreased through time, from 32% for the coseismic epoch to just 9% for pre-monsoon 2019, at least in part reflecting the decrease in the number of subsequent inventories that can be included in the analysis of each modelled epoch. For example, after the pre-monsoon 2019 model (Epoch 12), *Rout_Mod* cells could only be realized in Epoch 13, compared to a total of eight subsequent inventories (∼4.5 years) after the coseismic model (Epoch 4). However, this decrease in realization percentages is not monotonic, with a notable switching between pre- and post-monsoon positions in both 2016 and 2017 (Epochs 6–9) (Figures 6 and 7b), likely reflecting seasonal variability in landslide visibility as also detected in our multi-temporal inventory (Kincey et al., 2021).

3.4 | Regional-scale spatial distribution of modelled runout

Summarized by slope unit, coseismic landslide area is concentrated in a broad northwest-southeast zone (Kincey et al., 2021; Roback et al., 2018), aligned in particular with the physiographic divide between the Middle Hills, Middle Mountains and the High Himalaya (Figure 8a). The spatial distributions of coseismic *Rout_Mod* area (Figure 8b) and summed *p(Rout)* values (Figure 8c) broadly coincide with that zone (Figure 8a). The majority of slope units across the northern extent of the study area have a high ratio of *Rout_Mod* area to *Ls_Map* area (Figure 8d). However, the central high-relief region, around Rasuwa, Nuwakot and Sindhupalchok districts in particular (see Figure 1a for district names), has large areas of coseismic landsliding (Figure 8a) and notably lower ratios (Figure 8d). Ratio values are also markedly lower across slope units to the south of the study area, indicating that modelled runout from landslides in these locations was proportionally less extensive (Figure 8d).

The distribution of realized coseismic hazard, defined here as the percentage of coseismic *Rout_Mod* cells within a single slope unit that became *Rout_Real* in any post-seismic epoch, shows considerable spatial heterogeneity (Figure 9a). Clusters of contiguous slope units (typically < 5 connected units) with high *Rout_Real* percentages are present, but these are frequently adjacent to slope units with very low values, and there is little apparent spatial structure at the scale of our study area. The exception to this is a broad swathe of high values extending across Rasuwa, Nuwakot and Sindhupalchok. This again broadly mirrors the zone of highest densities of coseismic landsliding (Figure 8a), the highest summed *p(Rout)* values (Figure 8c), and some of the lowest *Rout_Mod* area to *Ls_Map* area ratios (Figure 8d). Maximum *p(Rout)* values per slope unit are only weakly correlated with the *Rout_Real* coseismic percentages (Figure 9b), showing that runout realization is not limited to slope units with high runout susceptibilities.
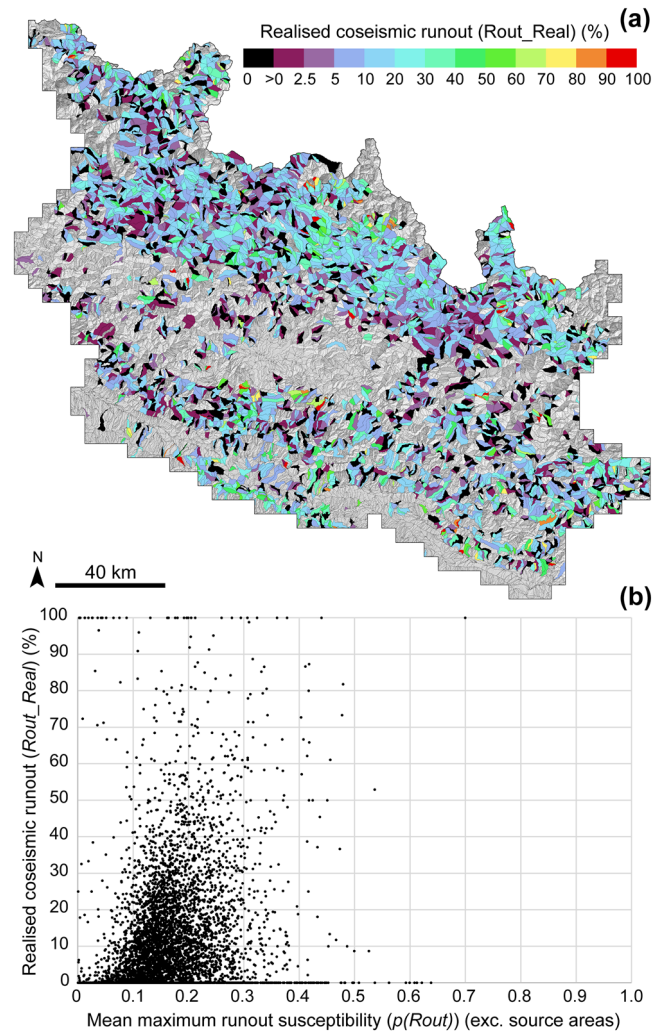
FIGURE 9 (a) Realized coseismic runout (*Rout_Real*) plotted by individual slope unit. Values indicate the percentage of cells in each slope unit that were modelled as part of the coseismic runout area (*Rout_Mod*), and were then occupied by a landslide in any post-seismic epoch (*Ls_Map*). (b) Scatterplot of per-slope unit realized coseismic runout (*Rout_Real*) (%) against the mean of all maximum runout susceptibility (*p(Rout)*) values within each corresponding slope unit. Note: Data are only plotted for slope units that include runout cells. [Color figure can be viewed at wileyonlinelibrary.com]

3.5 | Controls on changing post-earthquake runout characteristics

No clear correlations are apparent at slope unit level between the topographic variables (Section 2.4) and the percentage values of realized coseismic hazard (*Rout_Real*), suggesting that any potential causal relationships are likely to be manifest below slope unit scale. In contrast, at 10 m resolution, the kernel density estimate differencing of these variables shows marked variation between *Rout_Mod* cells for which the hazard was realized within 4.5 years after the earthquake, and cells for which it was not (Figure 10). Modelled runout cells where the hazard became realized preferentially occurred at elevations above approximately 2750 m, and in particular between 3500 and 5000 m (Figure 10a), whereas at lower elevations (< 2750 m) *Rout_Mod* was markedly less likely to be realized. Similarly, realized runout preferentially occurred at slope angles > 35°, with a modal peak at 45°, but much less frequently for lower slope angles
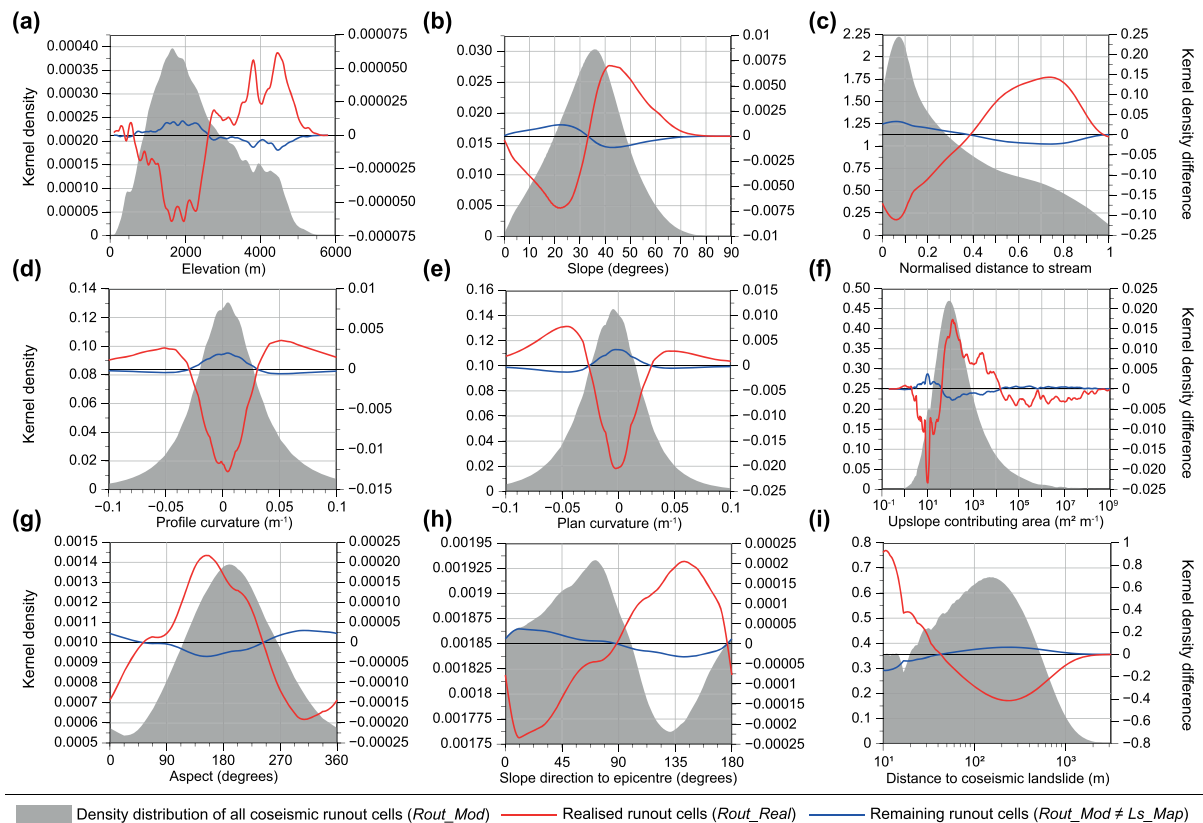
FIGURE 10 Kernel density distributions of all modelled coseismic runout cells (*Rout_Mod*) for selected topographic, seismic and distance-based variables. Differences in kernel density values relative to the overall distribution are shown for those cells where the coseismic runout hazard was later realized (*Rout_Real*; red) and for those where it was not (*Rout_Mod* ≠ *Ls_Map*; blue). Shaded areas show distributions of each variable for all coseismic runout cells (*Rout_Mod*) within the study area for reference. [Color figure can be viewed at wileyonlinelibrary.com]

(Figure 10b). When analysed across a normalized hillslope profile, *Rout_Mod* cells were more likely to become *Rout_Real* in the middle-upper portion of the slope (normalized distance from hillslope toe of 0.4–0.9) than in hillslope toe locations (Figure 10c).

Modelled runout cells were preferentially realized during the study period on hillslopes which are strongly curved in both profile (Figure 10d) and plan (Figure 10e), as compared to planar hillslopes. For profile curvature, this occurred where slopes are upwardly convex with values < -0.03 m^{-1} and upwardly concave with values > 0.03 m^{-1}, while for plan curvature realized cells were preferentially on concave slopes where flow is convergent (< -0.025 m^{-1}) and convex slopes where flow is divergent (> 0.03 m^{-1}). Upslope contributing area shows a complex relationship to realization, which was most likely to occur at values between 500 and 100,000 m^2 (Figure 10f).

Rout_Mod cells that experienced landslides over the study period also preferentially occurred on slopes with aspects between approximately 90° and 240°, representing hillslopes facing orientations between east, south and west-southwest, with a modal peak around south-southeast (Figure 10g). *Rout_Real* cells on more northerly-facing slopes were noticeably less common. When aspect is adjusted to reflect hillslope direction relative to the Gorkha earthquake epicentre, the distribution shows that realized runout was preferential on slopes facing obliquely away (90°–175°), despite these hillslopes being relatively infrequent in the study area (Figure 10h), and in contrast, *Rout_Mod* cells on slopes facing the epicentre generally did not become *Rout_Real*. Realized runout also preferentially occurred close

to coseismic *LS_map* cells, especially for distances < 50 m (Figure 10i). Beyond this distance, *Rout_Mod* cells were much less likely to experience landslides in subsequent epochs, suggesting that realization of the modelled runout extent was mainly achieved via iterative extension of coseismic landslides, rather than via the occurrence of entirely new landslides in downslope locations.

4 | DISCUSSION

Post-earthquake landsliding can represent a significant secondary hazard in the months and years after mountain region earthquakes. A considerable portion of this hazard arises from the remobilization of previously failed material, and so understanding the evolution of the associated runout holds the potential to locate, and therefore mitigate, this component of post-earthquake hazard. Our results provide the first regional-scale assessment of how this runout hazard changes in the years following a large continental earthquake, including the extent to which the overall potential runout area is realized and what local factors control the degree to which this occurs.

4.1 | Evolution of landslide runout following a large earthquake

Our results demonstrate that the overall area modelled to be at risk of runout from mapped landslides increased considerably after the 2015

Gorkha earthquake. The area at risk of potential runout peaked after the 2015 monsoon, but importantly remained above coseismic levels through the end of the 2019 monsoon (Figure 2). This pattern of runout susceptibility fits with our understanding of the changing pattern of landslides following this earthquake, which suggests that the overall landslide footprint remained large through at least 2019 relative to coseismic levels (Kincey et al., 2021; Rosser et al., 2021). Our results are in contrast with those of Dahlquist and West (2019), who documented a rapid decline in debris-flow activity after the Gorkha earthquake and suggested that the transient increase in debris flow rates did not persist beyond 2016.

There are several possible reasons for the apparent differences in these two studies. One important consideration is that our modelling is based on all visible landslides in each epoch (Kincey et al., 2021), as opposed to mapping only newly-occurring landslides (Dahlquist & West, 2019). Since we have no data on sediment availability or volume, our approach makes the conservative assumption that any existing landslide could potentially be a source of future runout. The peak in runout susceptibility after the 2015 monsoon therefore reflects the transition from more landslides being triggered than revegetated, to more landslides revegetating than being triggered, rather than an actual peak in landslide rate. It is certain that some of the landslides that persisted as bare ground in post-seismic inventories will in fact have been already exhausted of readily mobile sediment and so will no longer pose an immediate hazard in terms of secondary runout. This means that our time series represents a precautionary scenario that will likely overestimate hazard persistence relative to studies that only document new or substantially-altered source areas. However, we know that the majority of coseismic landslide deposits remain in place on hillslopes for years after a large earthquake, with estimates for Wenchuan ranging between 80 to 90% of the initially mobilized material still being in situ after 6–7 years (Dai et al., 2021; Fan, Domènech, et al., 2018; Huang & Li, 2014; Märki et al., 2021; Zhang & Zhang, 2017). Even though the proportion of this material that is readily erodible will decrease through time (Domènech et al., 2019; Qu, 2019; Yunus et al., 2020), longer-term studies have demonstrated that elevated rates of debris flows can persist for decades (Li et al., 2018; Ni et al., 2019).

Similarly, enhanced rates of new post-seismic landsliding will persist in the years after a large earthquake, meaning that the source areas available for remobilization will also evolve (Dadson et al., 2004; Li et al., 2018; Zhang et al., 2016), and that new locations will become susceptible to runout (Zhang & Zhang, 2017). Defining the period over which both new post-seismic landslides and post-seismic runout play out needs to balance the likely period over which the earthquake legacy remains relevant for the failure of new landslides and the time for the landscape to experience forcing from a full spectrum of conditions that drive remobilization. Analysis of landsliding during the 2020 monsoon, which was recognized as intense in the area of the 2015 earthquake, suggests that the legacy of the Gorkha earthquake has persisted at least that long (Rosser et al., 2021).

Importantly, our results also demonstrate that the overall potential runout extent can be estimated as a multiple of the mapped landslide area (Figure 3), thereby helping to constrain the potential magnitude of the runout phase of the overall cascading hazard. Modelled runout areas are on average four times larger than equivalent landslide areas for the pre- and coseismic periods, but five times

larger for post-seismic inventories (Figures 2 and 3). This change in runout-to-source area ratio (*Rout_Mod:Ls_Map*) could reflect differences in the hillslope location and topographic characteristics of post-seismic landslides, which are often at higher elevations (Fan, Domènech, et al., 2018; Kincey et al., 2021) and on steeper slopes (Li et al., 2018; Yunus et al., 2020) than pre-seismic landslides, and so have greater potential for longer runout pathways. The similarity between the coseismic and pre-seismic runout-to-source ratios is likely the result of a combination of factors, including that coseismic landslides are typically larger, rounder in plan and, at least after the Gorkha earthquake, were less channelized than pre- or post-seismic landslides (Kincey et al., 2021). As post-seismic landsliding progressively shifts towards a dominance of rainfall triggering, the ratio between *Rout_Mod* area and *Ls_Map* area should also decrease, a trend which may be occurring from post-monsoon 2016 (Epoch 7) onwards (Figure 3).

4.2 | Realization timescales associated with modelled runout susceptibility

Our results show that 14% of all modelled coseismic runout cells, equivalent to 85 km², experienced a landslide at some point within the 4.5 years following the earthquake (Figure 5a), and this proportion increases to 32% when the model output is thresholded by a susceptibility threshold that maximizes the model precision. We find that 90% of the total runout realization extent originates from changes to pre-existing coseismic landslides, and only 10% from entirely new landslides within the modelled runout footprint (Figure S14). This total realization area is equivalent to 57% of the total area affected by coseismic landsliding as a result of the 2015 Gorkha earthquake. Analysis of the rate at which coseismic *Rout_Mod* cells become *Rout_Real* shows a marked decrease through time, with 4.8% of the modelled runout area experiencing a landslide within 6 months of the earthquake, but just 0.3% of cells taking the full 4.5 years (Figure 6). This indicates that the majority of actual runout from coseismic landslides occurred in the immediate post-seismic period, with limited ongoing expansion of this extent continuing through time. These results mirror the short-lived mobilization of debris flows from coseismic landslides observed by Dahlquist and West (2019) by post-monsoon 2015. We would expect that the rate at which new runout occurred from coseismic landslides will continue to decrease through time, perhaps as sediment supply decreases (Qu, 2019), fine material is preferentially removed (Domènech et al., 2019), and stabilizing vegetation becomes re-established (Shen et al., 2020; Yang et al., 2018). This is reflected in the decreasing proportion of realized runout that relates to pre-existing landslides versus entirely new landslides for each of the post-seismic epochs (Figure S14).

The unrealized per-epoch percentage of coseismic *Rout_Mod* cells decreased consistently after the earthquake, from 81% in post-monsoon 2015 to just 50% by post-monsoon 2019 (Table S7), while the per-epoch percentage of coseismic *Rout_Mod* cells that ceased being hazardous increased from 15% in post-monsoon 2015 to 45% by post-monsoon 2019. This reduction in the total runout footprint reflects a decrease in the overall hazard from coseismic landslides through time. Since our results do not consider sediment supply or transport volumes, this decrease is solely the result of changes to

Ls_Map areas over time. It is important to note, however, that this pattern of change is based solely on the coseismic landslide inventory and does not include the potentially significant influence of new post-seismic landsliding (Kincey et al., 2021). This explains the apparent paradox that, although the *Rout_Mod* associated with coseismic landslides is decreasing through time (Figure 6; Table S7), the overall *Rout_Mod* area remains high (Figure 2). New landslides provide an additional supply of sediment that can subsequently be remobilized into debris flows (Zhang & Zhang, 2017). Analysis of runout realization for landslides in the post-monsoon 2015 inventory shows that 12% (95 km^2) of the modelled runout area experienced a landslide by the end of the time series, with this proportion remaining above 10% through 2016 and 9% for 2017, before decreasing rapidly after this date (Figure 7). Over the same time period, 0.3% of the study area experienced landslides, of which 39% lay inside and 61% lay outside the modelled runout area, although these values include the occurrence of new unconnected landslides as well as runout from existing landslides. Although the decreasing proportion of realization through time in part stems from the reduced number of post-epoch inventories included in the analysis of later model runs in the time series, the trend is not simply sequential. Interestingly, although there is some inter-epoch variability, realization rates for any given wait time decrease as the time series progresses (Figure 6), again suggesting that runout from post-seismic landslides occurs less frequently as more time elapses after the earthquake. Thus, the evolution of post-seismic runout hazard must be viewed as a palimpsest of overlapping susceptibilities from the inventory in each epoch, each decaying over time but superimposed on each other.

One important outstanding question is the degree to which the post-seismic runout realization timescale described earlier was determined by the timing of the earthquake itself. The Gorkha earthquake occurred in late April 2015, approximately 6 weeks before the start of the monsoon season and after a 6-month period of dry weather. This meant that the earthquake occurred in relatively dry hillslope conditions but immediately before the onset of the monsoon. It has been previously suggested that the antecedent moisture conditions at the time of an earthquake may influence the extent of coseismic landsliding (Marc et al., 2018). This has also been argued as one reason why some moderate earthquakes are able to generate more extensive coseismic landsliding, as in the case of the 2018 M_w 6.6 Hokkaido earthquake, which occurred 1 day after Typhoon Jebi (Cui et al., 2021; Wang et al., 2019). Given this, the degree to which landslides run out in the post-seismic period is influenced by their behaviour and runout at the time of the earthquake; wet coseismic landslides may immediately run out a considerable distance, or may develop as slower deeper-seated landslides; dry, blocky coseismic landslide deposits may remain perched in the landscape, or may avalanche, running out over long distances. In the case of the Gorkha earthquake, both landslide and runout areas peaked with the post-monsoon 2015 inventory (Figure 2), indicating that the intervening monsoon significantly increased the landslide runout across the earthquake-affected area. The pattern of *Rout_Real* wait times (Figure 6) in the following years shows a progressive reduction in the realization of modelled runout, overlaid with a high degree of epoch-by-epoch variation. Clarifying links between the seasonal timing of earthquakes and the pattern of coseismic and post-seismic landsliding and its runout should be a priority focus for future research.

4.3 | Controls on runout realization

When analysed at slope unit level, the spatial distribution of runout broadly reflects the distribution of coseismic landslides. Larger modelled runout extents are observed across much of the higher-relief areas to the north of the study area, although there is a notable region of low runout to source area ratios and high summed *p(Rout)* values coincident with the highest landslide densities, where the remaining hillslope area available to accommodate runout was limited (Figure 8). Despite pronounced spatial heterogeneity in the distribution of realized coseismic runout (Figure 9a), the percentage of realized hazard is again higher in those districts most badly affected by the earthquake. This indicates that slope units that experienced the highest densities of landsliding were also those in which post-seismic runout was most likely to occur, a finding that correlates with spatial variability in post-seismic activity after the Wenchuan earthquake (Ma et al., 2017; Ni et al., 2019). Whilst this may appear somewhat unsurprising, evidence of this tendency is important for focusing efforts within post-earthquake geohazard assessments. No correlation is present between those cells that transition from *Rout_Mod* to *Rout_Real* and mean maximum runout *p(Rout)* values (Figures 9b), and the lack of any clear correlations with topographic variables demonstrates that controls on runout are likely operating at the sub-slope unit scale. At a finer resolution (10 m cells), our results indicate a number of underlying physical controls that define where in the landscape is most susceptible to post-failure runout (Figure 10). This finding provides a significant step in the ability to anticipate locations that are more likely to experience post-seismic runout, and therefore where cascading hazard and associated risk is concentrated (Li et al., 2018; Tian et al., 2020; Zhang & Zhang, 2017).

Whilst the limited number of equivalent studies on the remobilization of coseismic and post-seismic landslides restricts a wider comparison of the controls on runout, our findings do correlate well with broader-scale assessments focusing on rates of new post-seismic landsliding and the reactivation of coseismic landslides (e.g., Fan, Domènech, et al., 2018). For example, we find that runout associated with coseismic landslides is most likely to be realized at elevations > 2750 m (Figure 10a). This is to be expected given that our results are showing progressive (downslope) runout from existing landslides, which themselves typically cluster at ridge-top locations (Meunier et al., 2008). Nevertheless, it is known that new post-seismic landsliding also tends to occur at higher average elevations than preceding coseismic landsliding (Fan, Domènech, et al., 2018; Khan et al., 2013; Kincey et al., 2021; Yunus et al., 2020), and so the distributions will also partially reflect the inclusion of entirely new landslides at higher elevations. Our finding that hazard realization preferentially occurs on steep slope angles of > 35° (Figure 10b) is also reflected by studies focusing on both post-seismic debris flows (Dahlquist & West, 2019) and post-seismic landsliding (Li et al., 2018; Yunus et al., 2020).

Locations in the middle-upper portion of the hillslope profile were also found to be more likely to be realized than those lower down the profile, or at the ridge top (Figure 10c). This at least in part reflects the spatial distribution of coseismic landslides, which tend to cluster towards ridge tops due to topographic amplification of seismic shaking (Meunier et al., 2008), and the downslope runout from these areas to mid-slope positions during post-seismic epochs. Mid-slope

positions are also likely to generate higher pore pressures and thicker overland flows, which are known debris flow triggers, as compared to ridge tops. This differs from patterns of new post-seismic landsliding after the Gorkha earthquake, which occurs more broadly across the entire hillslope profile but with a concentration towards lower hillslope positions (Kincey et al., 2021), where high pore fluid pressure is also present and undercutting of hillslopes may be more prevalent (Densmore & Hovius, 2000). In addition, we find that realization is more likely to occur on slopes with a pronounced degree of plan or profile curvature, notably for either convex and concave slopes (Figures 10d,e), and that realization is most likely for cells with an upslope contributing area of between 40 and 15,000 m^2 m^{-1} (Figure 10f). Whilst inferring an underlying mechanism for concentrating landslides in these areas from these data alone is challenging, the landslide distribution may reflect a combination of flow accumulation within concavities, and a reduction in slope stability around convexities, which both reduce the local factor of safety. According to our observations, remobilization and runout concentrate where there are most likely to be notable changes to flow characteristics (i.e., local concavities or convexities). Low contributing areas correspond to ridge top positions with limited landslide material available for remobilization, while very high contributing areas correspond to valley floors or lower portions of the channel network where slope may be a limiting factor in remobilization.

Aspect-dependent asymmetry in the distribution of landslide activity has been previously documented for both coseismic (Meunier et al., 2008) and post-seismic (Fan, Domènech, et al., 2018; Kincey et al., 2021) landslide inventories, and here we show that this signal is also manifest in runout. *Rout_Real* is preferentially concentrated on hillslopes oriented between east, south and west-southwest (Figure 10g), and on slopes facing away from the direction of the Gorkha epicentre (Figure 10h). These distributions may reflect a superimposition of directional asymmetry in the hillslope damage legacy generated by seismic shaking (Brain et al., 2017; Robinson et al., 2017), which influences where newly-failed ground may occur, and the dominant direction of prevailing monsoonal rains from the south-southeast in this part of the Himalaya, which combined may act to amplify the apparent directional preference for runout seen here (Fan, Domènech, et al., 2018). We also demonstrate that *Rout_Mod* cells proximal to pre-existing coseismic landslides, notably those within 50 m, are considerably more likely to be realized than those further away (Figure 10i). This finding indicates that runout is dominated by changes occurring over relatively short distances close to existing landslides, rather than more extensive runout over long distances, although the risk of more extensive runout should not be ignored. This pattern of activity concentrated near to existing landslides mirrors ideas around path dependency observed in other multi-temporal landslide inventories (Samia et al., 2017).

4.4 | Integrating runout evolution into long-term hazard and risk management

Landslide-triggering earthquakes in mountain regions can leave a concerning legacy of unstable slopes and extensive landslide debris, which compounds the risks faced by populations whose priority is reconstruction (Oven et al., 2021; Rieger, 2021). Any effort to

understand these complex hazards, and their evolution in time, is therefore of value. Whilst our capacity for regional-scale evaluation of individual hillslope susceptibility to new landslides after an earthquake is currently extremely limited, a potentially knowable risk is that posed by runout from coseismic landslide deposits in the landscape. Such remobilization commonly and tragically can lead to significant losses in the aftermath of large earthquakes, as has been seen in central Nepal since 2015 (Rosser et al., 2021).

In this research we argue that considerable gains can be made by isolating and characterizing the risks posed by the potential for runout from coseismic and post-seismic landslides, as this may represent a substantial portion of total landslide risk faced in the aftermath of a large earthquake. The need to model and map these risks is also clear: the long hillslopes, confined valley topography and complex drainage networks that are common in central Nepal often mean that upslope landslide hazards may not always be recognized, particularly where populations may have variable degrees of awareness of the hazards in the landscape around them. The behaviour of post-earthquake landslides is also likely to sit at odds with the lived experience of residents, because earthquakes result in larger, more numerous, and more active landslides than may have been present prior to an earthquake (Oven et al., 2021; Rieger, 2021).

We demonstrate here that a considerable area of land (85 km^2) within the earthquake-affected area could have been recognized after the earthquake was at risk from runout, based upon a precautionary parameterization of Flow-R. We also show that the potential hazard associated with post-seismic runout may have a spatial extent up to five times that of the coseismic landslide footprint alone, and so must be a significant factor in post-earthquake land-use planning. Whilst only 14% of this full modelled coseismic runout extent was realized within the first 4.5 years, this represents a valuable demarcation of areas at risk that could be generated immediately after coseismic landslides have been either modelled (Robinson et al., 2017) or mapped (Williams et al., 2018). Importantly, our model was run at 10 m resolution over the full earthquake affected area, which is a resolution relevant to individual land holdings and buildings, allowing those potentially at risk to be identified.

We also show that choices involving small distances (< 50 m) can make a significant difference to exposure to runout of landslide debris, and so this fine-scale information is critical for the selection of safer places for reconstruction. The tendency for landslide debris to channelize during runout poses a particular set of risks for valley bottom settlements, which commonly occupy the deposits of previous debris flows as these areas are often the only habitable land; identifying which of these areas are at greater risk where choices for development and reconstruction are highly limited is therefore essential. An important further finding of our work is that the runout hazard following a large earthquake changes significantly and in a complex manner through time as the contributing landslide sources also evolve. Identifying both where and critically when it is safe to rebuild is equally complex.

We took a precautionary approach to the modelling of potential runout in this study, assuming that any landslide visible as bare ground in any mapping epoch represented a possible source of future runout material. This approach was justified given the absence of any meaningful data relating to sediment volumes or supply across the earthquake-affected area, but it does mean that some source

locations that were already depleted of sediment will have been included within the analyses. Similarly, our approach to parameterizing and validating the model had to reflect the complexity and variability present within a landslide dataset that included > 190,000 source locations distributed across an area of > 24,000 km^2. A useful avenue for future research would therefore be to assess in more detail how the ideal parameterization of Flow-R changes through both space and time as the population of coseismic and post-seismic landslides evolve, including consideration of appropriate model susceptibility thresholds for different hazard and risk scenarios. In particular, analysing overall realization and model performance once the rate of runout and landsliding has returned to pre-seismic levels would allow model parameters to be better refined and a less precautionary hazard assessment produced. Repeating such analyses for other multi-temporal post-seismic landslide datasets would also provide important information on the degree to which standard model calibration can be applied within different topographic and seismic contexts.

Another important avenue for future research is linking the evolution of runout potential to the changes that occur in debris flow source material, mechanisms and initiation locations highlighted by other studies (e.g., Fan, Zhang, et al., 2018; Zhang et al., 2014; Zhang & Zhang, 2017). Crucially, future work should also consider the impacts of periodic high-intensity rainfall events on determining the trajectory and timing of runout evolution, with the large-scale modelling approach presented here providing the opportunity to assess whether localized triggering factors can explain the spatial variability in patterns of reactivation and runout documented elsewhere (Tang et al., 2016; Yunus et al., 2020). Including rainfall data of sufficient spatial and temporal resolution as part of the analysis of multi-temporal source inventories and modelling of runout pathways would generate invaluable information on how runout from coseismic landslides is likely to evolve under particular environmental conditions. Integrating such information into the planning framework associated with post-disaster response therefore has the potential to substantially improve our ability to forecast evolving cascading hazards and manage the associated risks.

5 | CONCLUSIONS

Using a spatially-distributed empirical sediment runout model, we considered how the spatial extent and relative likelihood of potential runout from existing landslides changed in the 4.5 years following the 2015 Gorkha earthquake in Nepal. Our results indicate that runout from coseismic landslides represents a considerable component of the overall mountain hazard chain, with actual runout representing an area equivalent to 57% of the total area impacted by coseismic landsliding, and the modelled potential runout area being on average 4–5 times the equivalent coseismic landslide area. Although the modelled runout area from the coseismic landslide population decreased through time, the overall runout potential remained high, indicating that the runout hazard is changing as a result of the evolution of the post-seismic landslide distribution itself. This finding clearly demonstrates the importance of developing systematic multi-temporal landslide inventories and associated runout susceptibility assessments in the years after a large earthquake.

Predicting the precise timing of runout from existing landslides remains problematic in the absence of high-resolution and accurate precipitation forecast data, an in-depth understanding of antecedent and local hillslope conditions, and extensive early warning systems. However, our results demonstrate the possibility to anticipate the spatial extent of future runout across an entire earthquake-affected area and to provide indicative timescales over which the runout is likely to occur. A comparison of modelled runout extents with subsequent mapped landslides shows that 14% of all modelled coseismic runout cells became landslides – which we term 'realization' of the hazard – at some point during the 4.5 years after the earthquake, equivalent to 85 km^2 of newly-affected ground. Limiting the modelled runout extent to higher susceptibility areas increases the model precision to 32% (10 km^2), meaning that the spatial location of a considerable area of potential future runout risk can be identified immediately after an earthquake using our precautionary approach to the modelling of secondary hazards.

Our analysis shows that the majority of runout realization occurs within the first 12 months after the earthquake, but that runout activity still persists after 4.5 years, reflecting both a lag in the subsequent mobilization of existing landslide debris and the occurrence of new landslides within modelled runout zones. Over the time period of our analysis, there are no clear correlations between the degree of hazard realization and a range of potential factors controlling landslide behaviour at the level of individual geomorphological slope units. However, these same control factors do clearly influence the likelihood of runout realization at the local (c. 10 m) scale, providing important information to help guide post-seismic risk-sensitive land-use planning.

Our findings enhance understanding of the extent and timing of cascading hazards following high magnitude earthquakes in mountain regions. Such regional-scale modelling of runout susceptibility from existing landslides has the potential to refine prediction of where, and over what timescales, future runout may occur, thereby greatly improving our ability to inform how we manage long-term post-seismic cascading hazard and risk. Embedding this knowledge within frameworks of disaster planning and decision-making has the potential to significantly improve the effectiveness of post-event recovery and reconstruction.

AUTHOR CONTRIBUTIONS

Conceptualization: M. E. Kincey, N. J. Rosser, A. L. Densmore, T. R. Robinson, R. Shrestha, D. S. Pujara, P. Horton, Z. M. Swirad, K. J. Oven, K. Arrell. Funding acquisition: N. J. Rosser, A. L. Densmore. Methodology: M. E. Kincey, N. J. Rosser, A. L. Densmore, T. R. Robinson. Investigation: M. E. Kincey, N. J. Rosser, A. L. Densmore, T. R. Robinson, R. Shrestha, D. S. Pujara, Z. M. Swirad. Data curation: M. E. Kincey, N. J. Rosser. Formal analysis: M. E. Kincey, N. J. Rosser, A. L. Densmore, T. R. Robinson. Project administration: N. J. Rosser. Resources: N. J. Rosser, A. L. Densmore. Visualization: M. E. Kincey, N. J. Rosser. Software: P. Horton, M. E. Kincey, N. J. Rosser. Writing – initial draft: M. E. Kincey, N. J. Rosser, A. L. Densmore, T. R. Robinson. Writing – reviewing & editing: M. E. Kincey, N. J. Rosser, A. L. Densmore, T. R. Robinson, R. Shrestha, D. S. Pujara, P. Horton, Z. M. Swirad, K. J. Oven, K. Arrell.

DATA AVAILABILITY STATEMENT

ORCID

Mark E. Kincey https://orcid.org/0000-0002-9632-4223
Zuzanna M. Swirad https://orcid.org/0000-0002-3592-9739

REFERENCES

Aaron, J., McDougall, S. & Nolde, N. (2019) Two methodologies to calibrate landslide runout models. *Landslides*, 16(5), 907–920. Available from: https://doi.org/10.1007/s10346-018-1116-8

Alvioli, M., Guzzetti, F. & Marchesini, I. (2020) Parameter-free delineation of slope units and terrain subdivision of Italy. *Geomorphology*, 358, 107124. Available from: https://doi.org/10.1016/j.geomorph.2020.107124

Alvioli, M., Marchesini, I., Reichenbach, P., Rossi, M., Ardizzone, F., Fiorucci, F. et al. (2016) Automatic delineation of geomorphological slope units with r. slopeunits v1. 0 and their optimization for landslide susceptibility modeling. *Geoscientific Model Development*, 9(11), 3975–3991. Available from: https://doi.org/10.5194/gmd-9-3975-2016

Blahut, J., Horton, P., Sterlacchini, S. & Jaboyedoff, M. (2010) Debris flow hazard modelling on medium scale: Valtellina di Tirano, Italy. *Natural Hazards and Earth System Sciences*, 10(11), 2379–2390. Available from: https://doi.org/10.5194/nhess-10-2379-2010

Blais-Stevens, A. & Behnia, P. (2016) Debris flow susceptibility mapping using a qualitative heuristic method and flow-R along the Yukon Alaska highway corridor, Canada. *Natural Hazards and Earth System Sciences*, 16(2), 449–462. Available from: https://doi.org/10.5194/nhess-16-449-2016

Brain, M.J., Rosser, N.J. & Tunstall, N. (2017) The control of earthquake sequences on hillslope stability. *Geophysical Research Letters*, 44(2), 865–872. Available from: https://doi.org/10.1002/2016GL071879

Claessens, L., Heuvelink, G.B.M., Schoorl, J.M. & Veldkamp, A. (2005) DEM resolution effects on shallow landslide hazard and soil redistribution modelling. *Earth Surface Processes and Landforms*, 30(4), 461–477. Available from: https://doi.org/10.1002/esp.1155

Cui, Y., Bao, P., Xu, C., Ma, S., Zheng, J. & Fu, G. (2021) Landslides triggered by the 6 September 2018 mw 6.6 Hokkaido, Japan: An updated inventory and retrospective hazard assessment. *Earth Science Informatics*, 14(1), 247–258. Available from: https://doi.org/10.1007/s12145-020-00544-8

Dadson, S.J., Hovius, N., Chen, H., Dade, W.B., Lin, J.C., Hsu, M.L. et al. (2004) Earthquake-triggered increase in sediment delivery from an active mountain belt. *Geology*, 32(8), 733–736. Available from: https://doi.org/10.1130/G20639.1

Dahlquist, M.P. & West, A.J. (2019) Initiation and runout of post-seismic debris flows: Insights from the 2015 Gorkha earthquake. *Geophysical Research Letters*, 46(16), 9658–9668. Available from: https://doi.org/10.1029/2019GL083548

Dai, L., Scaringi, G., Fan, X., Yunus, A.P., Liu-Zeng, J., Xu, Q. & Huang, R. (2021) Coseismic debris remains in the orogen despite a decade of enhanced landsliding. *Geophysical Research Letters*, 48(19), e2021GL095850.

Densmore, A.L. & Hovius, N. (2000) Topographic fingerprints of bedrock landslides. *Geology*, 38(4), 371–374.

Domènech, G., Alvioli, M. & Corominas, J. (2020) Preparing first-time slope failures hazard maps: From pixel-based to slope unit-based. *Landslides*, 17(2), 249–265. Available from: https://doi.org/10.1007/s10346-019-01279-4

Domènech, G., Fan, X., Scaringi, G., van Asch, T.W., Xu, Q., Huang, R. & Hales, T.C. (2019) Modelling the role of material depletion, grain coarsening and revegetation in debris flow occurrences after the 2008 Wenchuan earthquake. *Engineering Geology*, 250, 34–44. Available from: https://doi.org/10.1016/j.enggeo.2019.01.010

Fan, R.L., Zhang, L.M., Wang, H.J. & Fan, X.M. (2018) Evolution of debris flow activities in Gaojiagou ravine during 2008–2016 after the Wenchuan earthquake. *Engineering Geology*, 235, 1–10.

Fan, X., Domènech, G., Scaringi, G., Huang, R., Xu, Q., Hales, T.C. et al. (2018) Spatio-temporal evolution of mass wasting after the 2008 M w 7.9 Wenchuan earthquake revealed by a detailed multi-temporal inventory. *Landslides*, 15(12), 2325–2341. Available from: https://doi.org/10.1007/s10346-018-1054-5

Fan, X., Scaringi, G., Korup, O., West, A.J., van Westen, C.J., Tanyas, H. et al. (2019) Earthquake-induced chains of geologic hazards: Patterns, mechanisms, and impacts. *Reviews of Geophysics*, 57(2), 421–503. Available from: https://doi.org/10.1029/2018RG000626

Fischer, L., Rubensdotter, L., Sletten, K., Stalsberg, K., Melchiorre, C., Horton, P. et al. (2012) Debris flow modeling for susceptibility mapping at regional to national scale in Norway. Proceedings of the 11th International and 2nd North American Symposium on Landslides, 3–8 June 2012, Banff, Alberta, Canada.

Holmgren, P. (1994) Multiple flow direction algorithms for runoff modelling in grid based elevation models: An empirical evaluation. *Hydrological Processes*, 8(4), 327–334. Available from: https://doi.org/10.1002/hyp.3360080405

Horton, P., Jaboyedoff, M. & Bardou, E. (2008) Debris flow susceptibility mapping at a regional scale. In: Locat, J., Perret, D., Turmel, D., Demers, D. & Leroueil, S. (Eds.) *Proceedings of the 4th Canadian conference on Geohazards*. Quebec, Canada: Canadian Geotechnical Society, Engineering Geology Division, 20–24 May 2008, pp. 339–406.

Horton, P., Jaboyedoff, M., Rudaz, B.E.A. & Zimmermann, M. (2013) Flow-R, a model for susceptibility mapping of debris flows and other gravitational hazards at a regional scale. *Natural Hazards and Earth System Sciences*, 13(4), 869–885. Available from: https://doi.org/10.5194/nhess-13-869-2013

Horton, P., Loye, A. & Jaboyedoff, M. (2009) Debris Flows and Avalanches Susceptibility Hazard Mapping for Pakistan – Modelling of the two pilot districts Muzaffarabad and Manshera. Technical report, Faculty of Geosciences and Environment, Institute of Geomatics and Risk Analysis, University of Lausanne, Switzerland.

Huang, R. & Li, W. (2014) Post-earthquake landsliding and long-term impacts in the Wenchuan earthquake area, China. *Engineering*

Geology, 182, 111–120. Available from: https://doi.org/10.1016/j.enggeo.2014.07.008

Jaboyedoff, M., Choffet, C., Derron, M.-H., Horton, P., Loye, A., Longchamp, C. et al. (2012) Preliminary Slope Mass Movements Susceptibility Mapping Using DEM and LiDAR DEM. In: Pradhan, B. & Buchroithner, M. (Eds.) *Terrigenous mass movements: Detection, modelling, early warning and mitigation using Geoinformation technology*. Berlin Heidelberg, Germany: Springer-Verlag, pp. 109–170.

Jacobs, L., Kervyn, M., Reichenbach, P., Rossi, M., Marchesini, I., Alvioli, M. et al. (2020) Regional susceptibility assessments with heterogeneous landslide information: Slope unit-vs. pixel-based approach. *Geomorphology*, 356, 107084. Available from: https://doi.org/10.1016/j.geomorph.2020.107084

Kappes, M.S., Gruber, K., Frigerio, S., Bell, R., Keiler, M. & Glade, T. (2012) The MultiRISK platform: The technical concept and application of a regional-scale multihazard exposure analysis tool. *Geomorphology*, 151, 139–155.

Kappes, M.S., Malet, J.P., Remaître, A., Horton, P., Jaboyedoff, M. & Bell, R. (2011) Assessment of debris-flow susceptibility at medium-scale in the Barcelonnette Basin, France. *Natural Hazards and Earth System Sciences*, 11(2), 627–641. Available from: https://doi.org/10.5194/nhess-11-627-2011

Khan, S.F., Kamp, U. & Owen, L.A. (2013) Documenting five years of landsliding after the 2005 Kashmir earthquake, using repeat photography. *Geomorphology*, 197, 45–55. Available from: https://doi.org/10.1016/j.geomorph.2013.04.033

Kincey, M.E., Rosser, N.J., Robinson, T.R., Densmore, A.L., Shrestha, R., Pujara, D.S. et al. (2021) Evolution of coseismic and post-seismic landsliding after the 2015 mw 7.8 Gorkha earthquake, Nepal. *Journal of Geophysical Research: Earth Surface*, 126, e2020JF005803.

Li, C., Wang, M. & Liu, K. (2018) A decadal evolution of landslides and debris flows after the Wenchuan earthquake. *Geomorphology*, 323, 1–12. Available from: https://doi.org/10.1016/j.geomorph.2018.09.010

Li, G., West, A.J., Densmore, A.L., Hammond, D.E., Jin, Z., Zhang, F., Wang, J. et al. (2016) Connectivity of earthquake-triggered landslides with the fluvial network: Implications for landslide sediment transport after the 2008 Wenchuan earthquake. *Journal of Geophysical Research: Earth Surface*, 121(4), 703–724. Available from: https://doi.org/10.1002/2015JF003718

Losasso, L., Derron, M.-H., Horton, P., Jaboyedoff, M. & Sdao, F. (2016) Definition and mapping of potential rockfall source and propagation areas at a regional scale in Basilicata region (southern Italy). *Rendiconti Online Della Società Geologica Italiana*, 41, 175–178. Available from: https://doi.org/10.3301/ROL.2016.122

Ma, C., Wang, Y., Hu, K., Du, C. & Yang, W. (2017) Rainfall intensity–duration threshold and erosion competence of debris flows in four areas affected by the 2008 Wenchuan earthquake. *Geomorphology*, 282, 85–95. Available from: https://doi.org/10.1016/j.geomorph.2017.01.012

Marc, O., Behling, R., Andermann, C., Turowski, J.M., Illien, L., Roessner, S. et al. (2019) Long-term erosion of the Nepal Himalayas by bedrock landsliding: The role of monsoons, earthquakes and giant landslides. *Earth Surface Dynamics*, 7(1), 107–128. Available from: https://doi.org/10.5194/esurf-7-107-2019

Marc, O., Stumpf, A., Malet, J.P., Gosset, M., Uchida, T. & Chiang, S.H. (2018) Initial insights from a global database of rainfall-induced landslide inventories: The weak influence of slope and strong influence of total storm rainfall. *Earth Surface Dynamics*, 6(4), 903–922. Available from: https://doi.org/10.5194/esurf-6-903-2018

Märki, L., Lupker, M., France-Lanord, C., Lavé, J., Gallen, S., Gajurel, A.P., Haghipour, N. et al. (2021) An unshakable carbon budget for the Himalaya. *Nature Geoscience*, 14(10), 745–750.

Melo, R. & Zêzere, J.L. (2017) Modeling debris flow initiation and run-out in recently burned areas using data-driven methods. *Natural Hazards*, 88(3), 1373–1407. Available from: https://doi.org/10.1007/s11069-017-2921-4

Meunier, P., Hovius, N. & Haines, J.A. (2008) Topographic site effects and the location of earthquake induced landslides. *Earth and Planetary Science Letters*, 275(3–4), 221–232. Available from: https://doi.org/10.1016/j.epsl.2008.07.020

Michoud, C., Derron, M.H., Horton, P., Jaboyedoff, M., Baillifard, F.J., Loye, A. et al. (2012) Rockfall hazard and risk assessments along roads at a regional scale: Example in Swiss Alps. *Natural Hazards and Earth System Sciences*, 12(3), 615–629. Available from: https://doi.org/10.5194/nhess-12-615-2012

Ni, Z., Yang, Z., Li, W., Zhao, Y. & He, Z. (2019) Decreasing trend of geo-hazards induced by the 2008 Wenchuan earthquake inferred from time series NDVI data. *Remote Sensing*, 11(19), 2192–2222. Available from: https://doi.org/10.3390/rs11192192

Oppikofer, T., Hermanns, R., Sandøy, G., Böhme, M., Jaboyedoff, M., Horton, P. et al. (2016) Quantification of casualties from potential rock-slope failures in Norway. In: *Landslides and engineered slopes. Experience, theory and practice*. Leiden, The Netherlands: CRC Press, pp. 1537–1544.

Oven, K.J., Rana, S., Basyal, G.K., Rosser, N. & Kincey, M. (2021) Governing landslide risk in post-earthquake Nepal: Reflections on policy, politics and the meaning of place. In: Hutt, M., Liechty, M. & Lotter, S. (Eds.) *Epicentre to aftermath: Rebuilding and remembering in the wake of Nepal's earthquakes*. Delhi: Cambridge University Press. Available from: https://doi.org/10.1017/9781108991636.007

Parker, R.N., Hancox, G.T., Petley, D.N., Massey, C.I., Densmore, A.L. & Rosser, N.J. (2015) Spatial distributions of earthquake-induced landslides and hillslope preconditioning in the northwest South Island, New Zealand. *Earth Surface Dynamics*, 3(4), 501–525. Available from: https://doi.org/10.5194/esurf-3-501-2015

Pastorello, R., Michelini, T. & d'Agostino, V. (2017) On the criteria to create a susceptibility map to debris flow at a regional scale using flow-R. *Journal of Mountain Science*, 14(4), 621–635. Available from: https://doi.org/10.1007/s11629-016-4077-1

Paudel, B., Fall, M. & Daneshfar, B. (2020) GIS-based assessment of debris flow hazards in Kulekhani watershed, Nepal. *Natural Hazards*, 101(1), 1–30. Available from: https://doi.org/10.1007/s11069-020-03867-3

Pearce, A.J. & Watson, A.J. (1986) Effects of earthquake-induced landslides on sediment budget and transport over a 50-yr period. *Geology*, 14(1), 52–55. Available from: https://doi.org/10.1130/0091-7613(1986)14<52:EOELOS>2.0.CO;2

Qu, Y. (2019) Study on transformation rate of sources to debris flows in meizoseismal area. *Quaternary International*, 503, 51–58. Available from: https://doi.org/10.1016/j.quaint.2018.10.021

Rieger, K. (2021) Multi-hazards, displaced people's vulnerability and resettlement: Post-earthquake experiences from Rasuwa district in Nepal and their connections to policy loopholes and reconstruction practices. *Progress in Disaster Science*, 11, 100187. Available from: https://doi.org/10.1016/j.pdisas.2021.100187

Roback, K., Clark, M.K., West, A.J., Zekkos, D., Li, G., Gallen, S.F. et al. (2018) The size, distribution, and mobility of landslides caused by the 2015 Mw7. 8 Gorkha earthquake, Nepal. *Geomorphology*, 301, 121–138. Available from: https://doi.org/10.1016/j.geomorph.2017.01.030

Robinson, T.R. & Davies, T.R.H. (2013) Potential geomorphic consequences of a future great (M w= 8.0+) Alpine Fault earthquake, South Island, New Zealand. *Natural Hazards and Earth System Sciences*, 13(9), 2279–2299. Available from: https://doi.org/10.5194/nhess-13-2279-2013

Robinson, T.R., Rosser, N.J., Densmore, A.L., Williams, J.G., Kincey, M.E., Benjamin, J. et al. (2017) Rapid post-earthquake modelling of coseismic landslide intensity and distribution for emergency response decision support. *Natural Hazards and Earth System Sciences*, 17(9), 1521–1540. Available from: https://doi.org/10.5194/nhess-17-1521-2017

Rosser, N., Kincey, M., Oven, K., Densmore, A., Robinson, T., Pujara, D.S. et al. (2021) Changing significance of landslide Hazard and risk after the 2015 mw 7.8 Gorkha, Nepal earthquake. *Progress in Disaster Science*, 10, 100159. Available from: https://doi.org/10.1016/j.pdisas.2021.100159

Saito, T. & Rehmsmeier, M. (2015) The precision-recall plot is more informative than the ROC plot when evaluating binary classifiers on

imbalanced datasets. *PLoS ONE*, 10(3), e0118432. Available from: https://doi.org/10.1371/journal.pone.0118432

Samia, J., Temme, A., Bregt, A., Wallinga, J., Guzzetti, F., Ardizzone, F. et al. (2017) Do landslides follow landslides? Insights in path dependency from a multi-temporal landslide inventory. *Landslides*, 14(2), 547–558. Available from: https://doi.org/10.1007/s10346-016-0739-x

Shen, P., Zhang, L.M., Fan, R.L., Zhu, H. & Zhang, S. (2020) Declining geohazard activity with vegetation recovery during first ten years after the 2008 Wenchuan earthquake. *Geomorphology*, 352, 106989. Available from: https://doi.org/10.1016/j.geomorph.2019.106989

Tang, C., Van Westen, C. J., Tanyas, H. & Jetten, V. G. (2016) Analysing post-earthquake landslide activity using multi-temporal landslide inventories near the epicentral area of the 2008 Wenchuan earthquake. *Natural Hazards and Earth System Sciences*, 16(12), 2641–2655. Available from: https://doi.org/10.5194/nhess-16-2641-2016

Tanyas, H., Rossi, M., Alvioli, M., van Westen, C.J. & Marchesini, I. (2019) A global slope unit-based method for the near real-time prediction of earthquake-induced landslides. *Geomorphology*, 327, 126–146. Available from: https://doi.org/10.1016/j.geomorph.2018.10.022

Tian, Y., Owen, L.A., Xu, C., Ma, S., Li, K., Xu, X. et al. (2020) Landslide development within 3 years after the 2015 M w 7.8 Gorkha earthquake, Nepal. *Landslides*, 17(5), 1251–1267. Available from: https://doi.org/10.1007/s10346-020-01366-x

Wang, F., Fan, X., Yunus, A.P., Subramanian, S.S., Alonso-Rodriguez, A., Dai, L. et al. (2019) Coseismic landslides triggered by the 2018 Hokkaido, Japan (M w 6.6), earthquake: Spatial distribution, controlling factors, and possible failure mechanism. *Landslides*, 16(8), 1551–1566. Available from: https://doi.org/10.1007/s10346-019-01187-7

Williams, J.G., Rosser, N.J., Kincey, M.E., Benjamin, J., Oven, K.J., Densmore, A.L. et al. (2018) Satellite-based emergency mapping using optical imagery: Experience and reflections from the 2015 Nepal earthquakes. *Natural Hazards and Earth System Sciences*, 18(1), 185–205. Available from: https://doi.org/10.5194/nhess-18-185-2018

Yang, W., Qi, W. & Zhou, J. (2018) Decreased post-seismic landslides linked to vegetation recovery after the 2008 Wenchuan earthquake. *Ecological Indicators*, 89, 438–444. Available from: https://doi.org/10.1016/j.ecolind.2017.12.006

Yunus, A.P., Fan, X., Tang, X., Jie, D., Xu, Q. & Huang, R. (2020) Decadal vegetation succession from MODIS reveals the spatio-temporal evolution of post-seismic landsliding after the 2008 Wenchuan earthquake. *Remote Sensing of Environment*, 236, 111476. Available from: https://doi.org/10.1016/j.rse.2019.111476

Zhang, S., Zhang, L., Lacasse, S. & Nadim, F. (2016) Evolution of mass movements near epicentre of Wenchuan earthquake, the first eight years. *Scientific Reports*, 6(1), 1–9.

Zhang, S. & Zhang, L.M. (2017) Impact of the 2008 Wenchuan earthquake in China on subsequent long-term debris flow activities in the epicentral area. *Geomorphology*, 276, 86–103. Available from: https://doi.org/10.1016/j.geomorph.2016.10.009

Zhang, Y., Cheng, Y., Yin, Y., Lan, H., Wang, J. & Fu, X. (2014) High-position debris flow: A long-term active geohazard after the Wenchuan earthquake. *Engineering Geology*, 180, 45–54. Available from: https://doi.org/10.1016/j.enggeo.2014.05.014

SUPPORTING INFORMATION

Additional supporting information can be found online in the Supporting Information section at the end of this article.